



## **Short-to-Intermediate Slender Pin-Ended Cold-Formed Steel Equal-Leg Angle Columns: Experimental Investigation and DSM Design**

A. Landesmann<sup>1</sup>, D. Camotim<sup>2</sup>, Pedro B. Dinis<sup>2</sup> and R. Cruz<sup>1</sup>

### **Abstract**

Angles exhibit a complex structural behavior, responsible for the fact that, in the current North American Specification for Cold-Formed Steel Structures, short-to-intermediate equal-leg angle columns are (i) not yet pre-qualified for the Direct Strength Method (DSM) design and (ii) excluded from the application of the LFRD resistance factor  $\phi=0.85$ , valid for all other cold-formed steel compression members. Recently, the specific behavioral features exhibited by the above angle columns were incorporated into the proposal of a novel DSM-based design approach, for both fixed-ended and pin-ended columns, and it was shown that this added rationality goes along with quite accurate and reliable failure load predictions. However, the investigation leading to this design proposal also unveiled that there are no available experimental failure loads of slender pin-ended columns with intermediate-to-high slenderness values, which implied that the design procedure was validated for such columns exclusively on the basis of numerical failure loads. The research work reported in this paper provides a contribution towards filling this gap, since it mainly consists of an experimental study, carried out at the Federal University of Rio de Janeiro, on the behavior and collapse of short-to-intermediate slender pin-ended cold-formed steel equal-leg angle columns. After addressing the selection of the columns to be tested, the experimental set-up and test procedure are described in detail and the results obtained are presented and discussed. Such results involve (i) initial imperfection measurements, (ii) equilibrium paths relating the applied load to key column displacements, (iii) deformed configurations (including the collapse mode) and (iv) failure loads. Next, those same experimental results are used to validate a shell finite model previously developed by the authors, which is subsequently employed to obtain additional numerical failure load data concerning the pin-ended angle columns under scrutiny. Then, attention is turned to assessing the merits of the novel design approach. The comparison between the experimental and numerical values obtained in this work and their estimates provided by the design equations shows a very good correlation, perfectly in line with that observed in the recent studies available in the literature – this means that the validation and calibration of the above design approach may be deemed (successfully) completed. Finally, the paper closes with the presentation and assessment of small alterations to the existing design expressions, aimed at improving their accuracy and rationality, thus paving the way towards codification in the near future.

### **1. Introduction**

In spite of their geometrical simplicity, angle members, namely columns, are characterized by an extremely complex structural response, which has defied researchers and engineers for quite a long time.

---

<sup>1</sup> Civil Engineering Program, COPPE, Federal University of Rio de Janeiro, Brazil. <alandes; renatoevangelista@coc.ufrj.br>

<sup>2</sup> CERis, ICIST, DECivil, Instituto Superior Técnico, Universidade de Lisboa, Portugal. <dcamotim; dinis@civil.ist.utl.pt>

Although the non-linear behavior, strength and design of angle columns has attracted a lot of attention for decades (*e.g.*, Kitipornchai & Chan 1987, Kitipornchai *et al.* 1990, Popovic *et al.* 1999, Young 2004, Ellobody & Young 2005, Rasmussen 2005, 2006, Chodraui *et al.* 2006, Maia *et al.* 2008, Shifferaw & Schafer 2011, and Mesacasa Jr. 2012), it was not until the last few years that the mechanics underlying the column non-linear behavior were unveiled and properly understood (Dinis *et al.* 2012, Mesacasa *et al.* 2014) and it became clear why the current North American Specification (NAS) for Cold-Formed Steel Structures (AISI 2012) still excludes short-to-intermediate equal-leg angle columns from (i) the pre-qualification for the Direct Strength Method (DSM) design and (ii) the application of the LFRD resistance factor  $\phi=0.85$ , valid for all other cold-formed steel compression members. It was found that, although such columns buckle in flexural-torsional modes associated with a critical load plateau, the corresponding post-critical strength reserve changes considerably along that same plateau, thus affecting significantly the column failure load. Moreover, there was also clear numerical evidence that the failure of most angle columns stems from the interaction between two global instabilities, namely major-axis flexural torsional and minor-axis flexural buckling, a rather unique fully global coupling phenomenon. Based on these findings, Dinis & Camotim (2015) very recently developed, validated and proposed a novel rational procedure for the DSM design of equal-leg angle columns with short-to-intermediate lengths, which is valid for both pin-ended and fixed-ended support conditions and was shown to yield quite accurate and reliable failure load predictions. However, the investigation leading to this design proposal also exposed the fact that there are no available experimental failure loads concerning slender pin-ended columns, thus meaning that the validation procedure for such columns involved exclusively numerical failure loads in the intermediate-to-high slenderness range.

The main objective of this work is to fill the gap identified in the previous paragraph, by reporting an experimental study carried out at the Federal University of Rio de Janeiro and concerning short-to-intermediate slender pin-ended cold-formed steel equal-leg angle columns. After presenting a brief overview of the DSM procedure proposed by Dinis & Camotim (2015), the paper addresses the careful selection of the columns to be tested (and also analyzed numerically by means of shell finite element simulations), describes in some detail the experimental set-up and procedure employed, and presents and discusses the results obtained. Such experimental results consist of (i) initial imperfection measurements, (ii) equilibrium paths relating the applied load to key column displacements, (iii) deformed configurations (including the collapse modes) and (iv) failure loads. Next, those same experimental results are used to validate a shell finite model previously developed by the authors, which is subsequently employed to obtain additional numerical failure load data concerning the pin-ended angle columns under scrutiny, but covering also the small and small-to-intermediate slenderness range. Then, attention is turned to assessing the merits of the aforementioned novel DSM design approach. The comparison between the failure load estimates provided by the appropriate strength equations and the experimental and numerical values obtained in this work shows a very good correlation, qualitatively similar to that observed earlier for all the other columns, which means that the validation and calibration of the above design approach may be deemed (successfully) completed. Finally, the paper closes with the presentation and assessment of a few small alterations to the existing design expressions, aimed at improving their accuracy and rationality, thus paving the way towards a proposal for codification that will be made in the near future.

## **2. Overview of the Novel DSM Design Approach for Angle Columns**

As mentioned above, Dinis & Camotim (2015) have recently developed, validated and proposed a novel rational DSM-based procedure for the design of thin-walled cold-formed steel fixed-ended and pin-ended equal-leg angle columns with short-to-intermediate lengths, which was shown to yield quite accurate and reliable failure load predictions. The main features of this design approach are the following:

- (i) It is based on the fact that short-to-intermediate angle columns fail in interactive modes combining major-axis flexural-torsional and minor-axis flexural deformations.
- (ii) It involves the use of (ii<sub>1</sub>) the currently codified DSM global design curve and (ii<sub>2</sub>) a set of genuine flexural-torsional strength curves, developed for columns with minor-axis bending fully prevented.
- (iii) The above flexural-torsional curves make it possible to capture the progressive erosion of the column post-critical strength as its length increases within the  $P_{cr}(L)$  curve plateau.
- (iv) The effective centroid shift effects, strongly affecting the pin-ended column failure loads (not the fixed-ended ones), are included in the design approach through a parameter  $\beta$ , which must also reflect the change in column flexural-torsional behavior along the length (within the  $P_{cr}(L)$  curve plateau).
- (v) The length dependence of the column flexural-torsional post-critical strength and effective centroid shift effects is quantified by means of a parameter  $\Delta_f$ , defined as

$$\Delta_f = \frac{f_{bt} - f_{cft}}{f_{cft}} \times 100 \quad (1)$$

where  $f_{bt}$  and  $f_{cft}$  are the pure torsional and major-axis flexural-torsional (critical) buckling stresses<sup>3</sup>. Such buckling stresses can be determined exactly by means of the analytical expressions

$$f_{bt} = G \frac{t^2}{b^2} + \pi^2 \frac{E \cdot t^2}{12(L/2)} \quad (2)$$

$$f_{bf} = \frac{\pi^2 E b^2}{6(L/2)^2} \quad (3)$$

$$f_{cft} = \frac{4}{5} \left( f_{bt} + f_{bf} - \sqrt{(f_{bt} + f_{bf})^2 - 2.5 f_{bt} f_{bf}} \right) \quad (4)$$

where  $b$ ,  $t$  and  $L$  are the column leg width, thickness and length, and  $E$  is the material (steel) Young's modulus – note that  $f_{bf}$  is the column pure major-axis flexural buckling stress (needed to calculate  $f_{cft}$ ).

The angle columns nominal strength against the interactive failure under consideration ( $f_{nfte}$ ) is given by

$$f_{nfte} = \begin{cases} \beta \cdot f_{ne} & \text{if } \lambda_{fte} \leq \left(0.5 + \sqrt{0.25 - b}\right)^{\frac{1}{2a}} \\ \beta \cdot f_{ne} \left(\frac{f_{cft}}{f_{ne}}\right)^a \left[1 - b \left(\frac{f_{cft}}{f_{ne}}\right)^a\right] & \text{if } \lambda_{fte} > \left(0.5 + \sqrt{0.25 - b}\right)^{\frac{1}{2a}} \end{cases} \quad \text{with } \lambda_{fte} = \sqrt{\frac{f_{ne}}{f_{cft}}} \quad (5)$$

$$a = \begin{cases} 0.001 \Delta_f^3 - 0.032 \Delta_f^2 + 0.250 \Delta_f + 0.400 & \text{if } \Delta_f \leq 5.0 \\ 0.001 \Delta_f + 0.970 & \text{if } \Delta_f > 5.0 \end{cases} \quad (6)$$

$$b = \begin{cases} 0.014 \Delta_f + 0.150 & \text{if } \Delta_f \leq 7.0 \\ 0.248 & \text{if } \Delta_f > 7.0 \end{cases} \quad (7)$$

<sup>3</sup> The use of this parameter stems from the fact that it was found that the length-dependence of the angle column structural response can be “measured” by the relative importance of major-axis flexure on the flexural-torsional buckling behavior (critical stress and buckling mode).

In this expressions, (i) the slenderness  $\lambda_{fie}$  is based on the column nominal strength against minor-axis flexural collapse ( $f_{ne}$ ), obtained from the codified DSM global design curve

$$f_{ne} = \begin{cases} f_y \left( 0.658^{\lambda_c^2} \right) & \text{if } \lambda_c \leq 1.5 \\ f_y \left( \frac{0.877}{\lambda_c^2} \right) & \text{if } \lambda_c > 1.5 \end{cases} \quad \text{with} \quad \lambda_c = \sqrt{\frac{f_y}{f_{cre}}} \quad (8)$$

where  $f_{cre}$  is the column minor-axis flexural buckling stress and  $f_y$  is the material (steel) yield stress, and (ii) the parameter  $\beta$  is obtained from

$$\beta = \begin{cases} 1 & \text{for fixed-ended columns} \\ \frac{0.68}{\left( \lambda_{fie} - c \right)^d} \leq 1 & \text{for pin-ended columns} \end{cases} \quad (9)$$

$$c = \begin{cases} -300 \Delta_f^3 + 110.0 \Delta_f^2 - 12.8 \Delta_f + 1.0 & \text{if } \Delta_f < 0.2 \\ -0.002 \Delta_f^2 + 0.200 \Delta_f + 0.480 & \text{if } 0.2 \leq \Delta_f < 5.0 \\ -0.001 \Delta_f - 0.565 & \text{if } \Delta_f \geq 5.0 \end{cases} \quad (10)$$

$$d = \begin{cases} 380.0 \Delta_f^3 - 140.0 \Delta_f^2 - 15.2 \Delta_f + 0.25 & \text{if } \Delta_f \leq 0.2 \\ -0.008 \Delta_f^2 + 0.094 \Delta_f + 0.712 & \text{if } 0.2 < \Delta_f < 5.0 \\ 0.001 \Delta_f + 0.977 & \text{if } \Delta_f \geq 5.0 \end{cases} \quad (11)$$

It is worth noting that (i) the letter “b” in Eqs. (5) and (7) should not be confused with the angle leg width and, since this work deals exclusively with pin-ended columns<sup>4</sup>, (ii) only the bottom expression in Eq. (9) is considered. Finally, note also that the column failure/ultimate loads are calculated as

$$P_n = A \cdot f_{nfte} \quad (12)$$

### 3. Column Selection

The first stage of this work consisted of careful selecting the cross-section dimensions and lengths of the pin-ended angle columns to be tested experimentally and analyzed numerically. First of all, it should be recalled that the support conditions of the pin-ended columns are characterized by (i) simple supports concerning minor-axis flexure, (ii) fixed supports concerning major-axis flexure, (iii) fully prevented torsional rotations and (secondary) warping, and (iv) one longitudinal displacement fully prevented and the other completely free<sup>5</sup>. The selection procedure involved sequences of buckling analyses, performed using codes GBTUL (mostly), based on Generalized Beam Theory (GBT) (Bebiano *et al.* 2008), and ANSYS (shell finite element analyses) (SAS 2012). Concerning the columns to be tested experimentally (the main purpose of this investigation), the aim was to identify equal-leg angle columns (i) with cross-section dimensions commonly used in practice, (ii) buckling in flexural-torsional modes (*i.e.*, with short-

<sup>4</sup> Recall that the designation “pin-ended” concerns only the support conditions associated with minor-axis bending. The support conditions related to torsion and major-axis bending are the same for the fixed-ended and pin-ended columns.

<sup>5</sup> In the numerical analyses, it is customary to have both column cross-sections free to move longitudinally, while blocking the axial displacement of one point of the mid cross-section.

to-intermediate lengths), and exhibiting intermediate-to-high slenderness values ( $1.5 \leq \lambda_{fte} \leq 3.5$ ). In addition, it was necessary to satisfy the experimental set-up and specimen fabrication restraints, namely (i) a testing machine that cannot accommodate specimens longer than about  $1350\text{mm}$  and (ii) structural sheets made of mild steel with nominal Young's modulus, Poisson's ratio and yield stress values equal to  $E=205\text{GPa}$ ,  $\nu=0.3$  and  $f_y=304.5\text{MPa}$ , respectively, and with nominal thickness  $t=1.55\text{mm}$ .

Fortunately, it was possible to fulfill the requirements listed in the previous paragraph and the selection procedure led to the various angle column geometries (leg widths and lengths – recall that  $t=1.55\text{mm}$ ) given in Table 1, which are divided in five sets, each of them sharing the same cross-section dimensions (*i.e.*, leg width) – the column designation indicates its leg width and length, both in  $\text{mm}$  (*e.g.*, column 50L1200 has a  $50\text{mm}$  leg width and a  $1200\text{mm}$  length). The table also provides the column (i) areas  $A$ , (ii) squash loads  $P_y=A \cdot f_y$  (for  $f_y=304.5\text{MPa}$ ), (iii) flexural-torsional (critical –  $P_{crft}$ ) and torsional ( $P_{bt}$ ) buckling loads, (iv)  $\Delta_f$  ratios (see Eq. (1)), (v) global failure load estimates  $f_{ne}$  and (vi) slenderness values  $\lambda_{fte}$  – note that one has  $1.30 \leq \lambda_{fte} \leq 3.23$ . For illustration purposes, Figs. 1(a)-(b) (i) show the  $P_{cr}$  vs.  $L$  ( $L$  in logarithmic scale) curves concerning the five cross-sections (*i.e.*, leg widths) considered and, on each of them, indicates the lengths of the columns selected. The close observation of the values given in Table 1 and the buckling results displayed in Figs. 1(a)-(b) prompts the following remarks:

- (i) As already expected (Dinis *et al.* 2010), each  $P_{cr}$  vs.  $L$  curve consists of (i<sub>1</sub>) an initial more or less horizontal plateau, associated with major-axis flexural-torsional buckling, followed by (i<sub>2</sub>) a fast descending branch, associated with minor-axis buckling.

**Table 1:** Column specimens to be tested: geometry, squash load, buckling loads,  $\Delta_f$ ,  $f_{ne}$  and  $\lambda_{fte}$  ( $t=1.55\text{mm}$  and  $f_y=304.5\text{MPa}$ ).

Column designation	$b$ (mm)	$L$ (mm)	$A$ (cm <sup>2</sup> )	$P_y$ (kN)	$P_{crft}$ (kN)	$P_{bt}$ (kN)	$\Delta_f$ (%)	$f_{ne}$ (MPa)	$\lambda_{fte}$
50L600	50	600	1.55	47.20	12.46	12.44	0.32	244.99	1.75
50L900		900			12.00	12.05	0.71	186.68	1.55
50L1200		1200			11.79	11.92	1.26	127.59	1.30
60L500	60	500	1.86	56.64	11.07	10.99	0.11	274.17	2.16
60L600		600			10.67	10.62	0.16	261.81	2.14
60L700		700			10.43	10.40	0.21	247.91	2.11
60L900		900			10.15	10.16	0.34	216.75	2.00
70L500	70	500	2.17	66.08	9.90	9.80	0.06	281.91	2.50
70L600		600			9.43	9.37	0.09	272.51	2.51
70L700		700			9.15	9.11	0.12	261.80	2.50
70L900		900			8.84	8.82	0.19	237.20	2.42
80L500	80	500	2.48	75.52	9.07	8.95	0.04	287.05	2.82
80L600		600			8.54	8.46	0.05	279.69	2.86
80L700		700			8.22	8.16	0.07	271.23	2.87
80L900		900			7.86	7.84	0.11	251.49	2.82
90L500	90	500	2.79	84.96	8.47	8.33	0.03	290.62	3.12
90L600		600			7.87	7.78	0.03	284.72	3.20
90L700		700			7.51	7.45	0.04	277.90	3.23
90L900		900			7.12	7.08	0.07	261.79	3.21

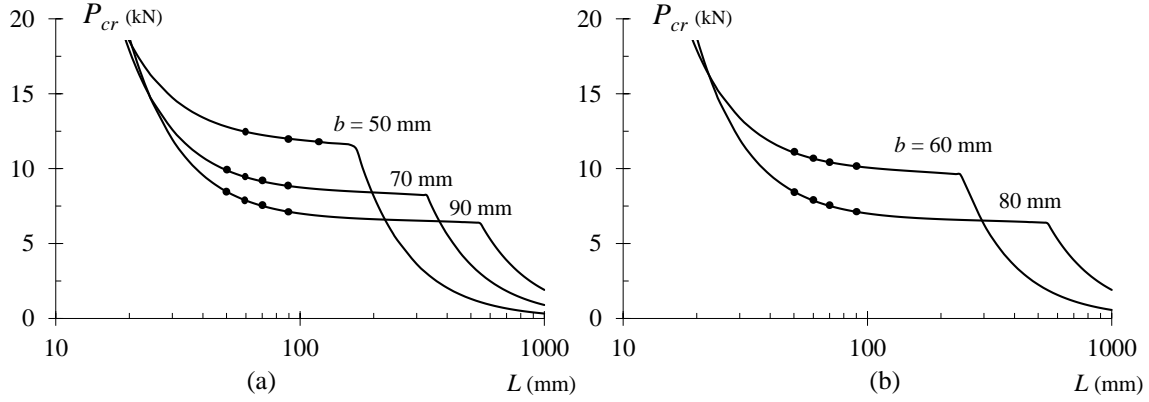


**Figure 1:** Curves  $P_{cr}$  vs.  $L$  concerning (a)  $b=50-70-90$  mm and (a)  $b=60-80$  mm columns, indicating the selected lengths.

- (ii) The column length corresponding to the transition from flexural-torsional buckling to flexural buckling increases with the leg width<sup>6</sup>. Indeed, for  $b=50-60-70-80-90$  mm, the above transition occurs for  $L=1600-2400-3500-4500-5600$  mm.
- (iii) For each cross-section dimensions, the value  $\Delta_f$  grows steadily with the column length.
- (iv) As mentioned before, the  $\lambda_{fte}$  values are comprised between 1.30 and 3.23, thus covering a fairly wide range. It is worth noting that, in general, quite high  $\lambda_{fte}$  values correspond to rather short columns – conversely, the longest column selected (50L1200) exhibits the lowest slenderness. In order to understand this apparently surprising feature, it is necessary to look at the definition of  $\lambda_{fte}$ , given in Eq. (5): it is the square root of the ratio between (iv<sub>1</sub>) the global strength  $f_{ne}$ , which decreases very fast with the column length, and (iv<sub>2</sub>) the flexural-torsional (critical) buckling stress  $f_{crft}$ , which exhibits a much less pronounced decrease with  $L$  (except for very short lengths). In order to illustrate the above assertion, Figs. 2(a)-(b) show, for the column with 70 mm wide legs, the variations with  $L$  of (iv<sub>1</sub>)  $f_{ne}$  and  $f_{crft}$ , and (iv<sub>2</sub>)  $\lambda_{fte}$  – the length range shown contains all the values selected. It is noted that the highest slenderness occurs for  $L \approx 620$  mm, which stems from the fact that (iv<sub>1</sub>)  $f_{ne}$  decreases continuously with  $L$ , (iv<sub>2</sub>) the  $f_{crft}$  vs.  $L$  curve displays a maximum at  $L < 100$  mm, followed by a very sharp drop until  $L \approx 360$  mm (from 200 MPa to about 50 MPa) and an almost horizontal plateau for longer columns. Thus, the highest  $f_{ne}/f_{crft}$  ratios occur for fairly short columns.

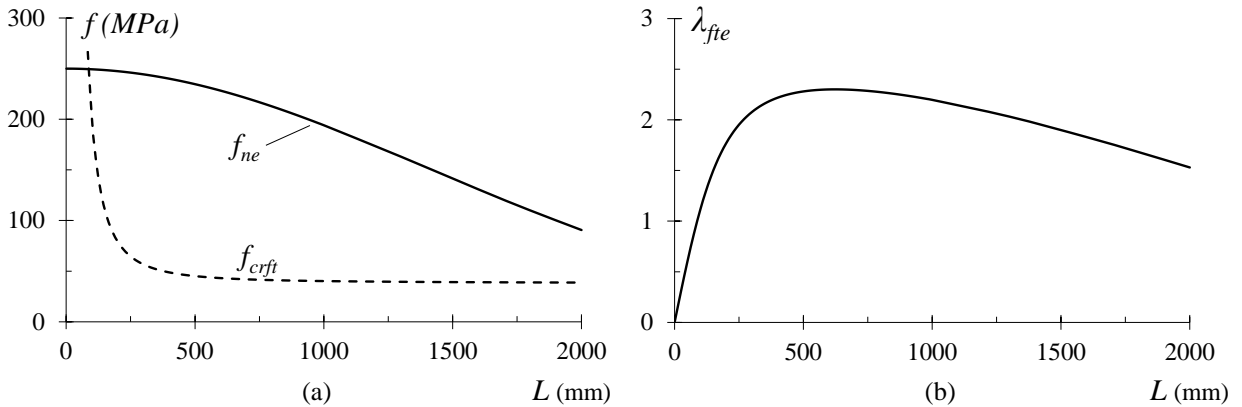


**Figure 2:** Variation with the length ( $0 \leq L \leq 2000$  mm) of (a)  $f_{ne}$  and  $f_{crft}$ , and (b)  $\lambda_{fte}$  for columns with 70 mm wide legs.

<sup>6</sup> In fact, the variation of the transition length correlates with the leg width-to-thickness ratio ( $b/t$ ). In this case, because the thickness remains unaltered, this correlation can be established solely with the leg width.

- (v) In order to assess the impact of the yield stress on  $\lambda_{fte}$ , Figs. 3(a)-(b) show, for column 70L900, the variations with  $f_y$  of (v<sub>1</sub>)  $f_{ne}$  and  $f_{crft}$ , and (v<sub>2</sub>)  $\lambda_{fte}$ . It is noted that increasing the yield stress only leads to a visible slenderness rise up to a certain value (e.g., it is not possible to reach  $\lambda_{fte}=3.5$ ).

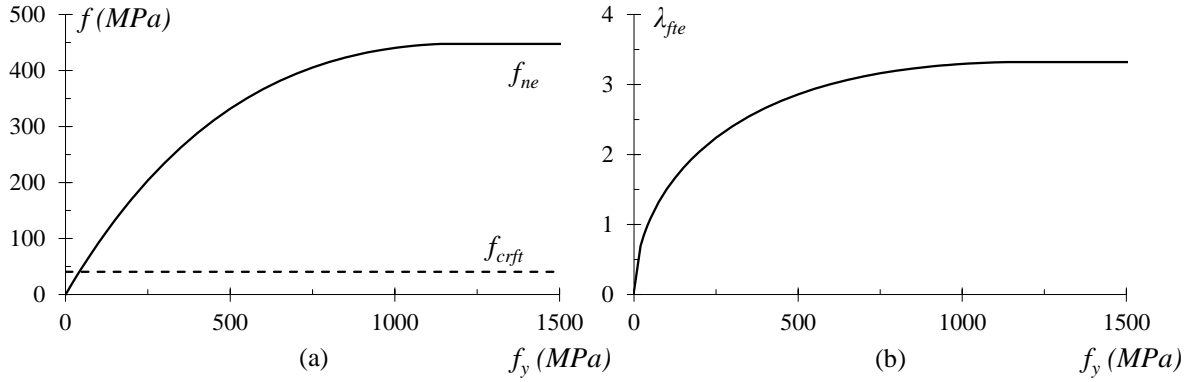


**Figure 3:** Variation with the yield stress ( $f_y \leq 1500$  MPa) of (a)  $f_{ne}$  and  $f_{crft}$ , and (b)  $\lambda_{fte}$  for the 70L900 column.

Concerning the columns to be analyzed numerically (just to obtain some additional failure load data), it was decided to consider the 19 columns selected previously, whose characteristics are given in Table 1, and vary their yield stresses, in order to widen the slenderness range covered. The yield stresses chosen were  $f_y=250-450-600$  MPa and Table 2 gives the column  $P_y, f_{ne}, \lambda_{fte}$  values – note that  $1.30 \leq \lambda_{fte} \leq 4.34$ .

**Table 2:** Column to be analyzed numerically (see also Table 1): yield stress, squash load,  $f_{ne}$  and  $\lambda_{fte}$ .

Column designation	$f_y$ (MPa)	$P_y$ (kN)	$f_{ne}$ (MPa)	$\lambda_{fte}$	$f_y$ (MPa)	$P_y$ (kN)	$f_{ne}$ (MPa)	$\lambda_{fte}$	$f_y$ (MPa)	$P_y$ (kN)	$f_{ne}$ (MPa)	$\lambda_{fte}$
50L600	250	38.75	209.1	1.62	450	69.75	326.3	2.02	600	93.00	390.9	2.21
50L900			167.3	1.47			218.4	1.68			228.4	1.72
50L1200			122.4	1.27			128.5	1.30			128.5	1.30
60L500		46.50	229.4	1.97		83.70	385.4	2.56		111.60	487.9	2.88
60L600			220.8	1.97			360.0	2.51			445.5	2.80
60L700			211.2	1.95			332.1	2.44			400.1	2.68
60L900			189.1	1.86			272.3	2.24			307.1	2.38
70L500		54.25	234.7	2.28		97.65	401.5	2.98		130.20	515.4	3.38
70L600			228.2	2.30			381.9	2.98			482.1	3.34
70L700			220.8	2.30			359.9	2.93			445.5	3.26
70L900			203.6	2.24			311.1	2.77			366.8	3.01
80L500		62.00	238.2	2.57		111.60	412.4	3.38		148.80	534.1	3.85
80L600			233.1	2.62			396.9	3.41			507.5	3.86
80L700			227.3	2.63			379.3	3.40			477.7	3.81
80L900			213.7	2.60			339.2	3.28			411.6	3.61
90L500		69.75	240.6	2.84		125.55	420.0	3.75		167.40	547.3	4.28
90L600			236.6	2.91			407.5	3.82			525.6	4.34
90L700			231.9	2.95			393.1	3.84			501.1	4.33
90L900			220.8	2.95			359.9	3.77			445.5	4.19

## 4. Experimental Investigation

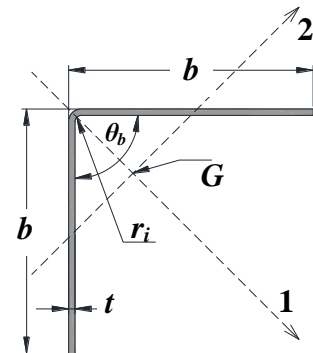
This section addresses the experimental investigation carried out at the Federal University of Rio de Janeiro – a more detailed account can be found in the work reported by Cruz (2015). Initially, the paper provides the characterization of the column specimens, which is followed by a description of the test set-up and procedure. Then, attention is devoted to presenting and discussing the experimental results recorded and/or observed before and during the tests, namely the specimen initial geometrical imperfections, measured displacements, equilibrium paths, failure loads and collapse mechanisms.

### 4.1 Column Specimens

The column specimens (i) were manufactured by press braking from zinc-coated structural sheets with nominal thickness  $t=1.55\text{ mm}$  and made of ZAR-345 mild steel, (ii) exhibited the five cross-section geometries given in Table 1 (nominal leg widths equal to 50-60-70-80-90 mm) and (iii) had lengths ranging from 500 to 1200 mm. Both ends were welded to 12 mm thick steel end-plates, which ensured full contact between the specimen end cross-sections and the test machine bearings. Table 3 provides the average values of the measured specimen leg width, thickness and length – also shown are the location of the cross-section centroid (G) and the principal axes (1-major and 2-minor). The specimen labeling is the same adopted in Table 1 and “R” identifies a repeated specimen (tested to assess the reliability of the experimental set-up and procedure). The cross-section dimensions were measured at five equally spaced locations along the measured specimen length  $L_0$  (0.00-0.25-0.50-0.75-1.00 $L_0$ ) and the values obtained were found to correlate very well with the nominal ones. Indeed, (i) the measured thickness values ranged from 1.55 to 1.59 mm and (ii) the ratios between the measured and nominal leg widths and lengths varied from 1.01 to 1.04 and from 0.99 to 1.02, respectively. The angles formed by the two angle legs ( $\theta_b$ ) were also measured at the above five specimen cross-sections and the average and standard deviation values obtained are equal to  $90.14^\circ$  and  $0.047$ , respectively. Finally, note that a press braking manufacturing condition imposed internal bending radii ( $r_i$ ) approximately equal to the sheet thickness  $t=1.55\text{ mm}$ .

**Table 3:** Average values of the measured column specimen cross-section dimensions, leg angles, lengths and areas.

Column	$b$ (mm)	$t$ (mm)	$\theta_b$ (deg)	$L_0$ (mm)	$A$ (cm <sup>2</sup> )
50L600	50.93	1.55	91.18	597	1.54
50L600-R	51.00	1.57	91.14	607	1.56
50L900	50.98	1.56	90.12	903	1.55
50L1200	51.22	1.58	90.02	1204	1.58
60L500	61.27	1.57	89.32	508	1.88
60L600	61.50	1.58	90.44	596	1.90
60L700	62.41	1.56	90.76	700	1.91
60L900	61.48	1.57	91.12	905	1.89
70L500	70.84	1.57	89.28	505	2.18
70L600	71.79	1.59	89.26	602	2.25
70L700	70.82	1.57	88.72	694	2.18
70L900	71.54	1.57	89.50	899	2.21
80L500	81.55	1.55	89.20	502	2.49
80L600	81.64	1.56	90.12	603	2.51
80L700	81.59	1.56	88.26	703	2.51
80L900	81.48	1.56	90.80	908	2.50
90L500	91.23	1.56	91.38	500	2.81
90L600	91.39	1.58	89.98	595	2.85
90L700	91.10	1.57	91.22	706	2.82
90L900	91.59	1.56	91.02	897	2.81



#### 4.2 Mechanical Properties of the Mild Steel

The mechanical properties of the structural ZAR-345 steel (ASTM 2011 or ABNT 2012) sheet employed to manufacture the column specimens were experimentally obtained by means of four standard tensile coupon tests. The coupons were extracted, longitudinally, from virgin steel sheets (belonging to the same batch of those used to manufacture the specimens) prior to the initiation of the cold-forming (press-braking) procedure. The coupon dimensions conformed to ASTM (2015) and ABNT (2015) for the tensile testing of metals:  $12.5\text{mm}$  wide coupons with  $50\text{mm}$  gauge length (“sheet-type”). Figs. 4(a)-(b) show a general view of a coupon tensile test and illustrate the experimental stress-strain-curves obtained. The tests were performed according to ASTM (2015) in a Shimadzu AGX-100kN displacement controlled universal testing machine (UTM) using friction grips. The longitudinal strains were measured through a  $50\text{mm}$  clip-on gage and two electrical strain gages, attached to each coupon face center (see Fig. 4(a)). A data acquisition system was used to record the load and strain readings at regular intervals during the tests ( $15\text{Hz}$ ). On the basis of the stress-strain curves determined experimentally, it was possible to obtain estimates of the steel mechanical properties – the corresponding average values are  $f_y=304.5\text{MPa}$  (yield stress),  $f_u=376.1\text{MPa}$  (ultimate stress) and  $E=205\text{GPa}$  (Young’s modulus)<sup>7</sup>. Moreover, a Poisson’s ratio  $\nu=0.3$  was always assumed.

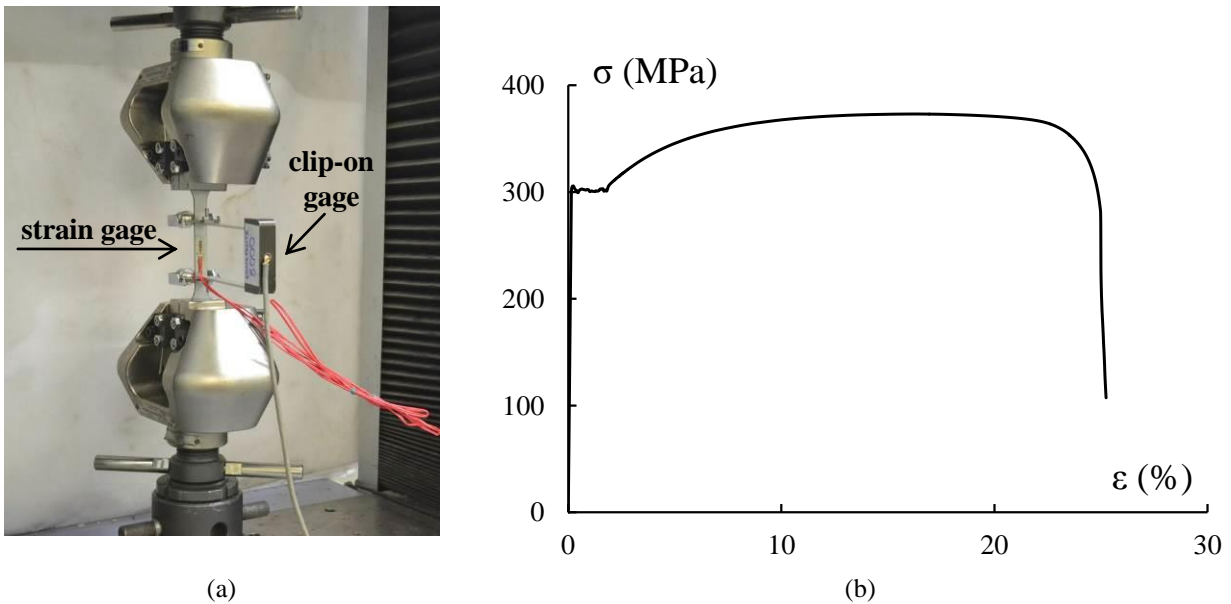


**Figure 4:** (a) General view of a coupon tensile test and (b) illustrative stress-strain curve experimentally obtained.

#### 4.3 Test Set-Up

All specimens were tested in an AMSLER 1mN servo-controlled hydraulic UTM under displacement-control conditions. The testing machine can supply compressive loads up to  $1000\text{kN}$  and the loads imposed during the performance of a test were measured with a  $50\text{N}$  accuracy and recorded in a data acquisition system. Fig. 5 provides an overall view of the test set-up, showing a moveable lower end support that allowed tests to be conducted for specimens with various lengths. As for Figs. 6(a)-(b), they provide a general view and schematic representations of the bottom (pinned) end support, formed by a pair of cylindrical hinges (i) built from machine-finished carbon steel and (ii) mounted on two  $12\text{mm}$  thick steel bearing plates – the top end support is similar. The end supports were designed to ensure null

<sup>7</sup> As stipulated in ASTM (2015), the yield stress corresponds to the onset of yielding and the ultimate stress is calculated by dividing the maximum load carried by the coupon during the tensile test by its original cross-section area.

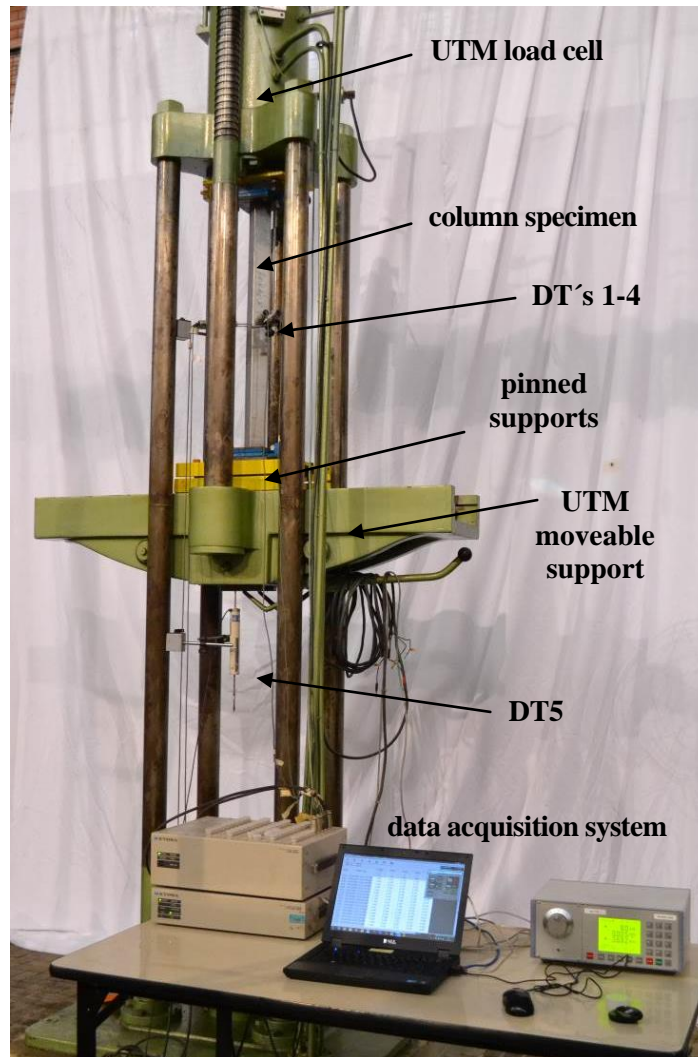


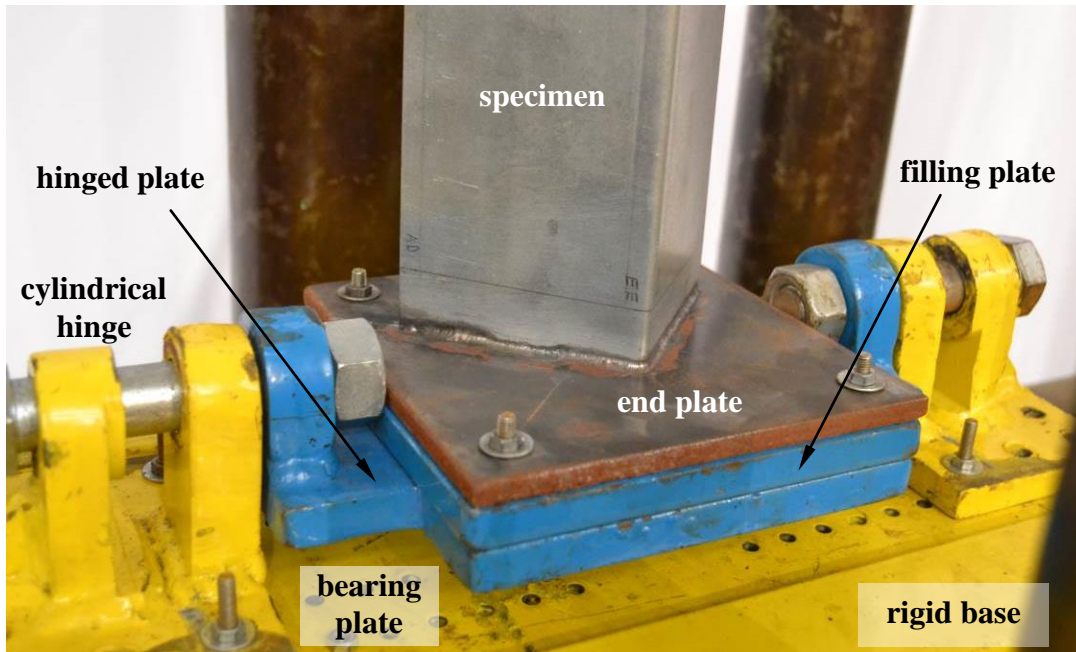
**Figure 5:** Overall view of the experimental test set-up and servo-controlled hydraulic UTM.

vertical distances between the specimen end cross-sections and the axes of rotation – this was achieved through the inclusion of “filling-plates” with adequate thickness (see Fig. 6(b))<sup>8</sup>. These end supports prevent (i) transverse displacements, (ii) major-axis flexural and torsional rotations, and (iii) secondary warping and local displacements/rotations (note that rigid plates are continuously welded to the specimen end cross-sections) – the corresponding support conditions are “fixed” with respect to major-axis flexure and torsion, and “pinned” with respect to minor-axis flexure.

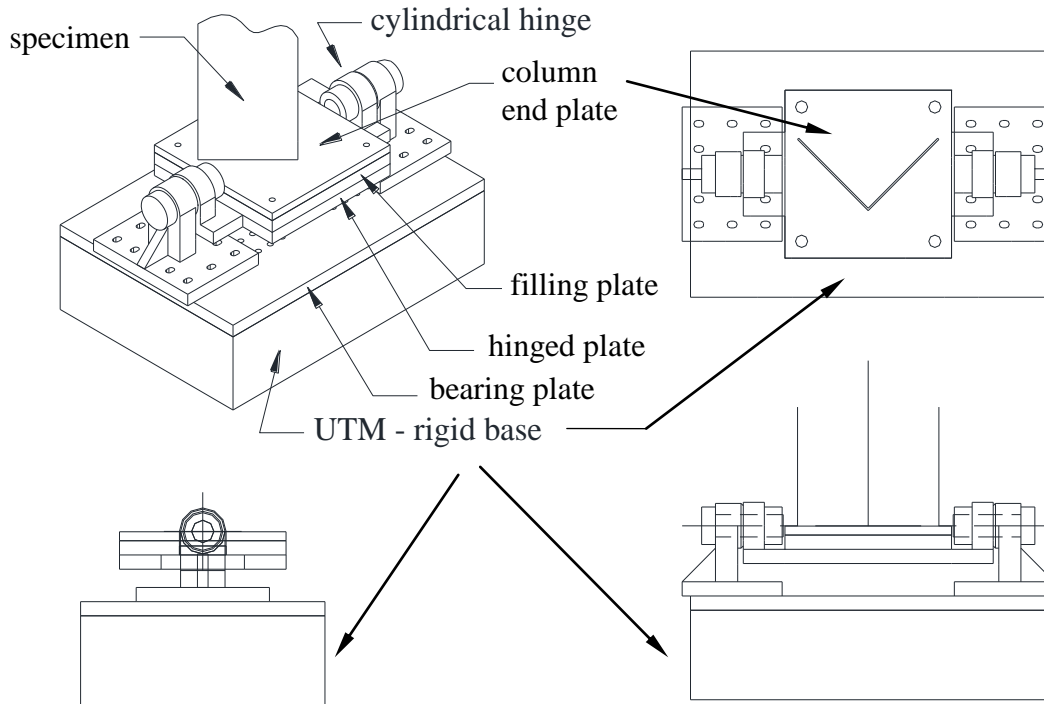
The welding of the specimen end cross-sections to the rigid plates is preceded by a very careful positioning procedure, aimed at achieving minute/negligible load eccentricities (lack of coincidence between the end cross-section centroids and the test frame loading axis). Such procedure involves the following steps:

- (i) The actual dimensions of the specimen end cross-sections are carefully measured, in order to enable an accurate definition of the real positions of their centroids.
- (ii) Each end cross-section shape and centroid location are properly marked on the end plate surface, so that the cross-section and plate centroids can be “perfectly aligned” longitudinally (see Fig. 7(a)).

<sup>8</sup> With this end support arrangement it is possible to guarantee the specimen minor-axis flexural buckling length coincides with its actual length, thus eliminating the need to consider a correction factor (Popovic *et al.* 1999 or Mesacasa *et al.* 2013).



(a)



(b)

**Figure 6:** Specimens bottom end support: (a) overall view and (b) schematic representations (3D, top, lateral and front views).

- (iii) After making sure that the centroids are coincident and the end plates are orthogonal to the specimen walls, the specimen end cross-sections are carefully TIG welded to the end plates along the whole contour, as shown in Fig. 7(b).

- (iv) Then, the specimen end plates are carefully bonded to the various plates providing the load transfer to the UTM rigid base, namely the filling, hinged and bearing plates (see Figs. 6(a)-(b)), making sure that their centroids are “perfectly aligned”. After ensuring the bond at the specimen bottom end support, the UTM actuator ram was moved slowly toward the specimen until the top hinged support arrangement (previously put in place and adequately bolted to the UTM loading plate, with the various plate centroids “perfectly aligned”) was in full contact with the specimen end plate. Then, once the appropriate horizontal positioning of the specimen is completed, the bottom support bolts are tightened and whole specimen positioning procedure is finished. In view of this careful procedure, it seems fair to argue that the tests are performed under virtually concentric loading conditions (the load eccentricity will certainly be extremely small and, therefore, can be neglected).

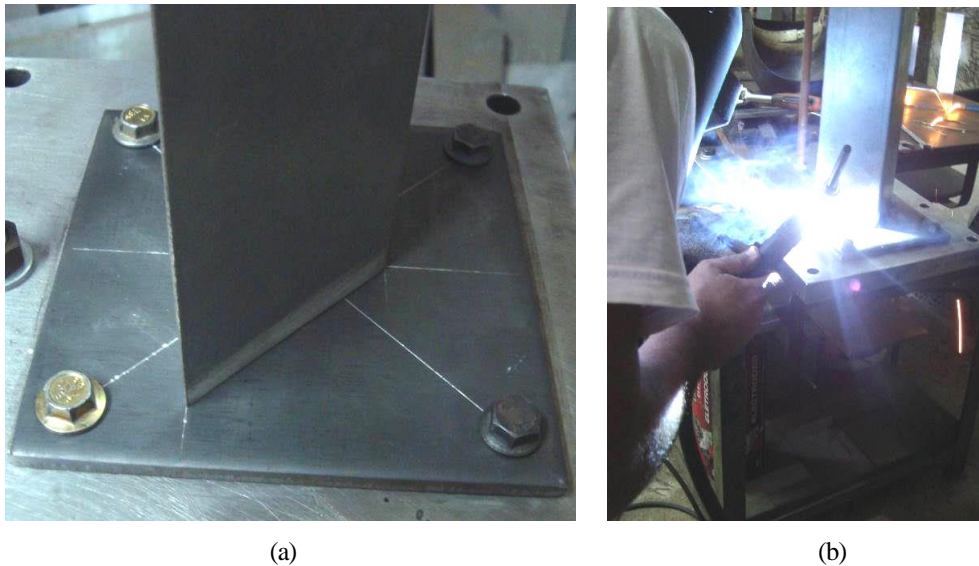
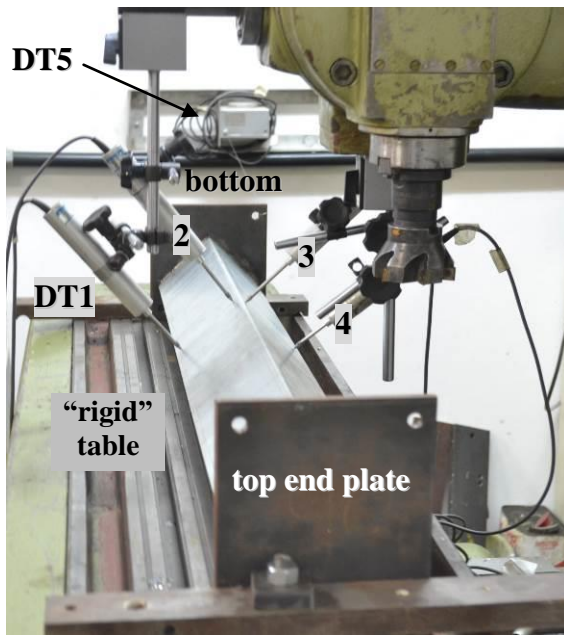


**Figure 7:** Rigid attachment of the specimen end cross-section to the end plate: (a) positioning and (b) continuously TIG welding along the whole contour.

#### 4.4 Displacement Measurements

Two sets of displacement measurements were made for each specimen, both of them by means of five displacement transducers (DTs) (i) able to move along the specimen outer surface prior to the test and (ii) placed at the specimen mid-height during the test. The DT arrangements (locations along the cross-section contour) involved in each set of displacement measurements are depicted in Figs. 8(a)-(b). The DT locations were carefully selected in order to enable capturing the column major-axis flexural-torsional and minor-axis flexural displacements, and can be characterized as follows:

- (i) The first arrangement concerns the measurement of the specimen initial geometrical imperfections (see Fig. 8(a)). Four DTs (DT1 to DT4) were supported by a (rigid) device mounted on a (also rigid) working table of a milling machine, which could move horizontally along the whole specimen length, guided and aligned by a transverse hand-wheel. The position was monitored by means of a fifth DT (DT5) wire potentiometer-type displacement transducer – Fig. 9 provides a view of this moving device, when attached to the specimen.
- (ii) The second arrangement involves four DTs (DT1-4 –see Fig. 8(b)), which provide measurements throughout the entire test duration, making it possible to assess the evolution of the specimen mid-height global displacements. An additional DT (DT5) was placed at the bottom face of the UTM moveable support device (see Fig. 5), to measure the specimen axial shortening.



(a)



(b)

**Figure 8:** DT arrangements to measure (a) initial geometrical imperfections and (b) mid-height displacements.

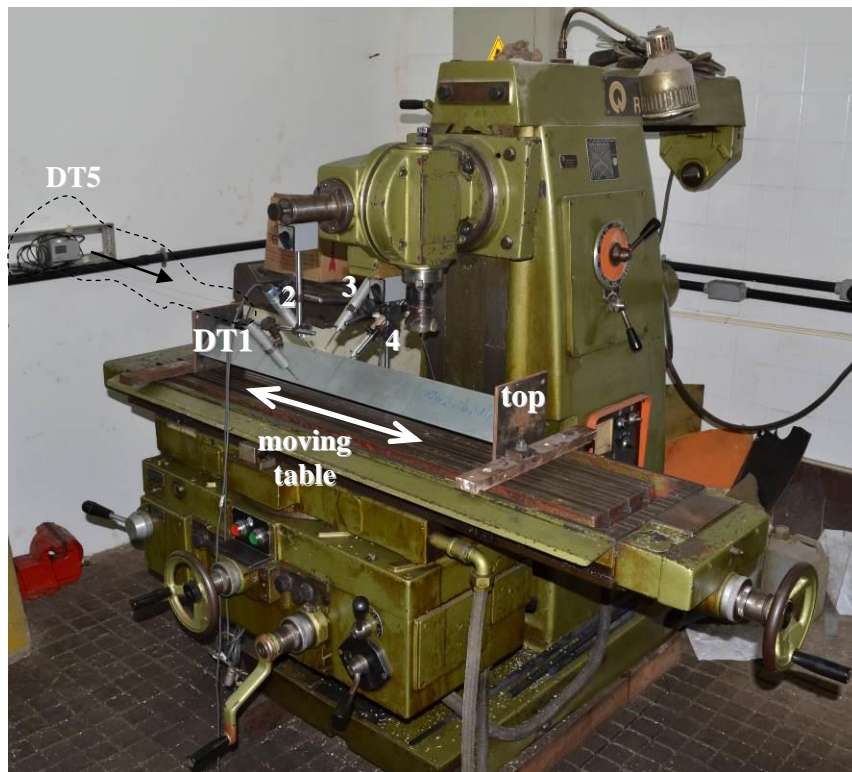


**Figure 9:** DTs involved in the measurement of the initial geometrical imperfections.

#### 4.5 Test Procedure

Each column specimen test involved the sequential performance of the following tasks:

- (i) TIG welding of 12mm thick steel plates to the specimen end cross-sections (Fig. 7(a)) and bolting each end plate to the corresponding test frame loading plate by means of four bolts (Figs. 5 and 6).
- (ii) Careful positioning of the specimen on the test frame, in order to achieve a vertical alignment “as perfect as possible” between the centroids of the (ii<sub>1</sub>) column end cross-sections, (ii<sub>2</sub>) column end plates, (ii<sub>3</sub>) support filling and hinged plates, and (ii<sub>4</sub>) UTM loading plate, thus ensuring minute (negligible) load eccentricity, *i.e.*, concentric compressive loading.
- (iii) Properly placing the five DTs transducers: four at the column mid-height (see Fig. 8(b)) and one at the UTM moveable support device bottom face (see Fig. 5).
- (iv) Slow (0.005mm/s) application of an initial small compressive load ( $\approx 1-2\text{ kN}$ ), in order to eliminate any possible gaps between the cylindrical end supports and the specimen bottom end plate.
- (v) Application of the displacement-controlled loading, by means of the UTM servo-controlled hydraulic actuator, at a sufficiently low rate to prevent the occurrence of relevant dynamic effects.
- (vi) Continuous recording, by means of a high frequency (15Hz) data acquisition system, of the mid-height DT (see Fig. 8(b)) outputs and the hydraulic actuator load cell readings.
- (vii) As the applied load approaches the anticipated column ultimate strength, the specimen deformed configurations are photographed, in order to obtain experimental evidence concerning the nature of the column failure mechanism, namely the occurrence of mode interaction.
- (viii) After the test, the recorded displacement and load measurements are post-processed to obtain the column experimental equilibrium paths and deformed configurations (including the failure mode), paying particular attention to the identification of the flexural and torsional deformations.

#### 4.6 Test Results

The experimental results obtained from this test campaign consist of column (i) initial geometrical imperfection configurations, (ii) equilibrium paths, relating the applied load to relevant displacements, (iii) failure load data and (iv) deformed configurations (including the failure mode) evidencing the presence of flexural and torsional deformations. Since the 20 column specimens tested shared essentially the same structural response, only a representative sample of these various types of experimental results are individually reported and discussed in the following subsections – the whole set of experimental results have been reported by Cruz (2015).

##### 4.6.1 Initial geometrical imperfections

Initial geometrical imperfections were measured by the spanning of transducers DT1 to DT4 (locations shown in Fig. 8(a)) along the specimen length. This was done for almost all the specimens, the exceptions being specimens 50L600-R and 50L1200 (the latter is longer than the milling machine table – see Fig. 9). Table 4 provides (i) the maximum and minimum values recorded, along the specimen length, by each transducer (DT1-4) and (ii) the computed values of the torsional rotation ( $\beta$ ) and translations due to major and minor-axis flexure ( $d_M$  and  $d_m$ , respectively). This computation (i) is based on the fact that the cross-sections undergo rigid-body motions and (ii) must take into account that the DT1-4 remain fixed while the measured cross-sections move (this also applies to the determination of the  $\beta$ ,  $d_M$  and  $d_m$  values due to the applied load – see Section 4.6.2) and was made by means of the procedure described next and illustrated in Figs. 10(a)-(c):

- (i) Fig. 10(a) shows an undeformed cross-section, lying on the X-Y plane, and the locations of the four DTs: (i<sub>1</sub>) DT1-2 are placed normally to the “vertical” leg at distances  $y_1=(b-10)\text{ mm}$  and  $y_2=10\text{ mm}$

**Table 4:** Measured and calculated maximum and minimum specimen initial displacement and rotation values

Column	DT1 (mm)	DT2 (mm)	DT3 (mm)	DT4 (mm)	$d_{M0}$ (mm)	$d_{m0}$ (mm)	$\beta_0$ (rad x $10^{-2}$ )
50L600	0.02/-0.42	0.43/0.00	0.24/-0.11	0.56/0.00	0.26/-0.11	0.56/-0.05	2.101/0.007
50L900	0.51/0.00	1.07/0.00	1.2/0.00	0.71/0.00.01	0.78/0.00	0.01/-0.17	0.59/0.346
60L500	0.13/-0.16	0.11/-0.01	0.11/0.00	0.59/-0.01	0.36/-0.01	0.12/-0.02	0.897/0.029
60L600	0.39/-0.23	0.43/0.00	0.00/-0.6	0.00/-0.14	0.25/-0.22	0.83/0.00	1.122/0.013
60L700	0.22/-0.42	3/-0.02	0.00/-0.49	0.06/-0.02	0.2/-0.3	2.65/0.00	3.754/0.125
60L900	0.53/-0.11	0.00/-0.14	0.00/-0.06	0.76/0.00.01	0.86/-0.01	0.05/-0.05	0.479/0.005
70L500	0.84/0.00	0.11/-0.01	0.88/-0.04	0.18/0.00	0.73/0.00	0.1/-0.83	0.103/1.536
70L600	0.77/-0.05	0.11/-0.04	0.00/-0.11	0.32/-0.43	0.76/-0.15	0.09/-0.02	0.017/0.607
70L700	1.6/0.00	0.36/0.00	0.2/-0.01	1.28/-0.05	2.04/-0.03	0.14/-0.07	0.217/0.47
70L900	1.04/-1.21	0.23/-0.18	0.49/-1.24	0.1/-0.03	0.81/-0.77	1.19/-0.44	2.431/1.247
80L500	0.06/0.00	0.1/0.00	0.45/-0.04	0.13/0.00	0.11/0.00	0.08/-0.31	0.081/0.253
80L600	0.18/-0.54	0.02/-0.11	0.01/-0.07	0.24/-0.04	0.12/-0.36	0.07/-0.06	0.534/0.162
80L700	2.49/0.00	0.45/0.00	0.69/-0.73	0.1/-0.04	1.74/0.00	0.67/-0.46	0.348/1.902
80L900	0.16/-0.8	0.22/-0.03	0.04/-0.16	0.00/-1.21	0.05/-1.39	0.1/-0.01	0.046/0.577
90L500	0.04/-1.14	0.04/-0.05	0.13/-0.48	0.05/-0.11	0.00/-0.88	0.47/-0.02	1.063/0.023
90L600	0.15/-0.86	0.19/-0.04	0.00/-1.25	0.01/0.00	0.1/-0.59	1.08/0.00	1.478/0.011
90L700	0.19/-1.07	0.19/0.00	0.5/-0.82	0.14/-0.12	0.2/-0.82	0.91/-0.3	1.395/0.27
90L900	0.18/-0.6	0.15/-0.08	0.23/-1.19	0.18/-0.04	0.25/-0.4	0.97/-0.12	1.146/0.081

from the corner, and (i<sub>2</sub>) DT3-4 are placed normally to the “horizontal” leg, at distances  $x_3=10mm$  and  $x_4=(b-10)mm$  from the corner. Because the DTs are fixed, the “horizontal” and “vertical” projections of these distances obviously vary as the cross-section deforms (see Fig. 10(b)). The signs of the displacements measured by the DTs are in accordance with the coordinate system  $x-y$  associated with the  $X-Y$  axes – moreover, the torsional rotation angles  $\beta$  are positive clockwise.

- (ii) The first step consists of using the four DT measurements to calculate the cross-section torsional rotation  $\beta$  and “horizontal” ( $d_H$ ) and “vertical” ( $d_V$ ) translations. Then, a coordinate change leads to the determination of the translations along the major ( $d_m$ ) and minor ( $d_M$ ), as indicated in Fig. 10(b).
- (iii) The cross-section torsional rotation  $\beta$  can be straightforwardly obtained from one of the expressions

$$\beta = \tan^{-1}\left(\frac{DT1 - DT2}{y_2 - y_1}\right) \quad \text{or} \quad \tan^{-1}\left(\frac{DT4 - DT3}{x_4 - x_3}\right) \quad (13)$$

- (iv) The determination of  $d_H$  and  $d_V$  is more involved, because it must account for the continuous (as deformation evolves) change in the relative position of the four DTs with respect to the cross-section, cross-section, as illustrated in Fig. 10(b). Each displacement measured by a DT combines two parts, one identical to a translation ( $d_H$  or  $d_V$ ) and the other equal to the product of the torsional rotation by an “horizontal” or “vertical” distance that depends on the cross-section corner location. Indeed, the measurements of DT1 and DT4 can be expressed in terms of  $d_H$ ,  $d_V$  and  $\beta$  as (see Fig. 10(b))<sup>9</sup>

<sup>9</sup> Note that the values of  $d_H$ ,  $d_V$  and  $\beta$  can be obtained from the measurements of only three DTs. The fourth DT measurement is used for verification purposes.

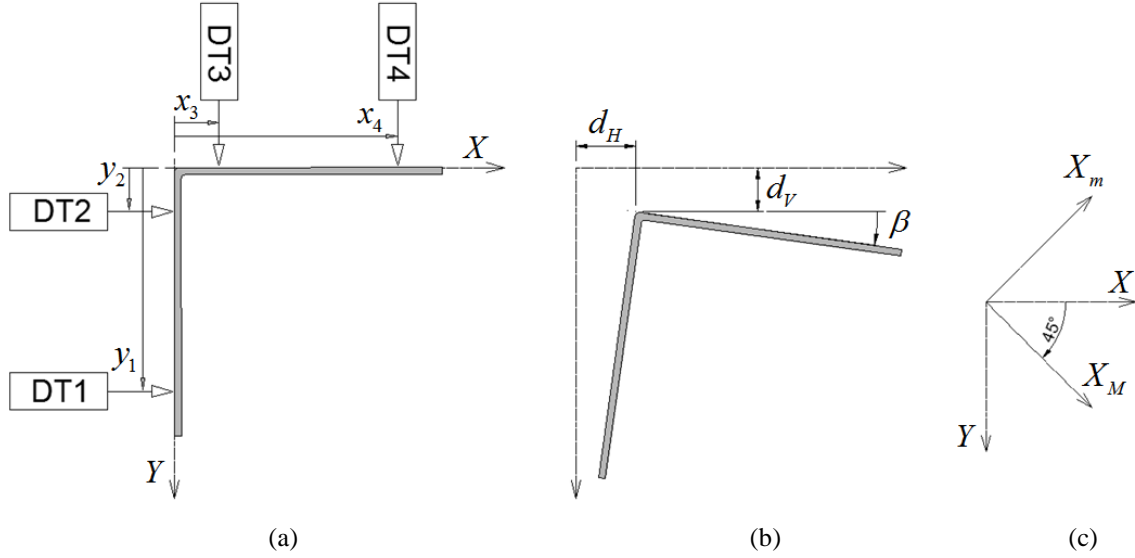


**Figure 10:** (a) Cross-section undeformed configuration and DT locations, (b) cross-section deformed configuration and definition of  $d_H$ ,  $d_V$  and  $\beta$ , and (c) change of coordinate axes, required to determine  $d_M$  and  $d_m$ .

$$DT1 = d_H - (y_1 - d_V) \tan \beta \quad (14)$$

$$DT4 = d_V + (x_4 - d_H) \tan \beta \quad (15)$$

- (v) Solving the system formed by Eqs (14) and (15) and taking into account Eq. (13), the values of  $d_H$  and  $d_V$ , defining the location of the cross-section corner, are obtained from the expressions

$$d_H = (DT1 - DT4 \tan \beta + y_1 \tan \beta + x_4 \tan^2 \beta) / (1 + \tan^2 \beta) \quad (16)$$

$$d_V = (DT1 \tan \beta + DT4 + y_1 \tan^2 \beta - x_4 \tan \beta) / (1 + \tan^2 \beta) \quad (17)$$

- (vi) The last step consists of expressing the location of the cross-section corner through its coordinates along the cross-section centroidal principal axes ( $d_M$  and  $d_m$ ), which form  $45^\circ$  angles with the “horizontal” and “vertical” – this straightforward procedure is illustrated in Fig. 10(c) and leads to<sup>10</sup>

$$d_M = (d_H + d_V) \sqrt{2} / 2 \quad (18)$$

$$d_m = (d_H - d_V) \sqrt{2} / 2 \quad (19)$$

As for Figs. 11(a)-(b), they show the initial displacement/rotation longitudinal profiles acquired from the tests involving specimens 60L500-600-700-900, which were obtained either (i) directly from DT1-4 readings or (ii) using Eqs. (13)-(15) ( $\beta$ ,  $d_M$  and  $d_m$ ) – note that (i) the horizontal coordinates are normalized with respect to the column measured length  $L_0$  ( $DT5/L_0$ ) and (ii) the sign assumed for the transducer readings is also indicated (positive/negative readings for outward/inward displacements, respectively). The observation of these results prompts the following remarks:

<sup>10</sup> Since  $d_M$  and  $d_m$  are defined as caused by major-axis and minor-axis bending, they consist of displacements taking place along the cross-section centroidal principal minor ( $X_m$ ) and major ( $X_M$ ) axes, respectively.

- (i) With two exceptions, the DT1-4 measurements are fairly low, as their maximum absolute value is about  $1.25\text{ mm}$ , *i.e.*, very close to the nominal wall thickness. The exceptions are the (i<sub>1</sub>) DT1 readings of  $1.6\text{ mm}$  and  $2.49\text{ mm}$ , for specimens 70L700 and 80L700, respectively, and (i<sub>2</sub>) DT2 readings of  $3.0\text{ mm}$ , for specimens 60L700.
- (ii) All displacement profiles provided by the DT1-4 readings exhibit (ii<sub>1</sub>) some degree of asymmetry and (ii<sub>2</sub>) a dominant single half-wave sinusoidal shape, combined with minor participations of two and three half-wave sinusoids.
- (iii) The maximum  $d_M$  and  $d_m$  values are also quite low: about  $2.04\text{ mm}$  and  $2.7\text{ mm}$ , respectively. Moreover, the  $d_M/L_0$  and  $d_m/L_0$  ratios (iii<sub>1</sub>) vary from  $2.14 \times 10^{-6}$  to  $2.91 \times 10^{-3}$ , and from  $5.51 \times 10^{-6}$  to  $3.78 \times 10^{-3}$ , respectively, and (iii<sub>2</sub>)  $L/1000$  is exceeded columns 70L500, 70L600, 70L700, 80L700, 80L900, 90L500 ( $d_M$ ), and 60L600, 60L700, 70L900, 90L600, 90L700, 90L900, 70L500 ( $d_m$ ). Finally, the mid-span torsional rotation  $\beta$  ranges between  $-1.902 \times 10^{-2}$  and  $3.754 \times 10^{-2}\text{ rad}$ .

#### 4.6.2 Equilibrium paths

Fig. 12 shows the equilibrium paths obtained from the test involving specimens 50L600-60L600-80L700, relating the applied load  $P$ , provided by the UTM hydraulic actuator load cell, to (i) the axial shortening  $\Delta$  (DT5 reading) and (ii) the mid-height torsional rotation  $\beta$  and translations due to minor-axis ( $d_m$ ) and major-axis ( $d_M$ ) flexure – the values of  $\beta$ ,  $d_m$  and  $d_M$  are caused by the applied load (*i.e.*, do not include the initial imperfections). The observation of such equilibrium paths lead to the following comments:

- (i) The equilibrium paths  $P$  vs.  $\Delta$  exhibit initial portions that are virtually linear and whose slopes are quite similar (difficult to distinguish), thus reflecting the relatively close column axial stiffness values –  $EA/L_0=528.8-653.5-731.9\text{ kN/cm}$  for the 50L600-60L600-80L700 columns. Moreover, note also that both the (i<sub>1</sub>) applied load level associated with the transition to a non-linear curve and (i<sub>2</sub>) length covered by such non-linear curve (prior to failure) vary considerably – they increase with the values of the column (i<sub>1</sub>) critical buckling load and (i<sub>2</sub>) parameter  $\Delta_f$  (see Table 1), respectively.
- (ii) The equilibrium paths  $P$  vs.  $\beta$  and  $P$  vs.  $d_M$  follow practically the same trend (accounting for the different scales, of course), which stems from the fact that they correspond to a single deformation pattern, akin to the flexural-torsional buckling mode. However, because this mode is predominantly torsional, the torsional rotations clearly overpower the major-axis flexural displacements.
- (iii) The equilibrium paths  $P$  vs.  $d_m$  only branch out of the null displacement vertical line at quite advanced loading stages. This is due to the fact that such displacements, which rapidly become much larger than their  $d_M$  counterparts, stem from a combination of (iii<sub>1</sub>) effective centroid shift effects, occurring in all columns, and (iii<sub>2</sub>) interaction with minor-axis flexural buckling, only relevant for columns with relatively close flexural-torsional and flexural buckling loads. In this case, the latter aspect has very little relevance, since  $f_{cft}$  and  $f_{cre}$  are very far apart in the tree columns (see Table A.1).
- (iv) The amount of deformation exhibited by the three sets of equilibrium paths  $P$  vs.  $\beta$ ,  $P$  vs.  $d_M$  and  $P$  vs.  $d_m$  prior to failure varies with  $\Delta_f$  (see Table 1), which is due to the influence of this parameter on the column post-critical strength and ductility prior to failure unveiled by Dinis *et al.* (2012). In the case of these three columns, all  $\Delta_f$  values are quite small (the 50L600 column one is the highest) and, therefore, the differences are not very perceptible and, moreover, can easily be “masked” by the different initial geometrical imperfections<sup>11</sup>.

<sup>11</sup> Dinis & Camotim (2015) performed an extensive parametric study, involving sets of columns with identical cross-section dimensions and initial geometrical imperfection shapes and amplitudes (only the length varied along the  $P_{cr}$  vs.  $L$  “plateau”). They showed clearly that, as the length moves along the “plateau” (*i.e.*,  $\Delta_f$  increases), the column post-critical strength and ductility prior to failure increase and decrease, respectively.

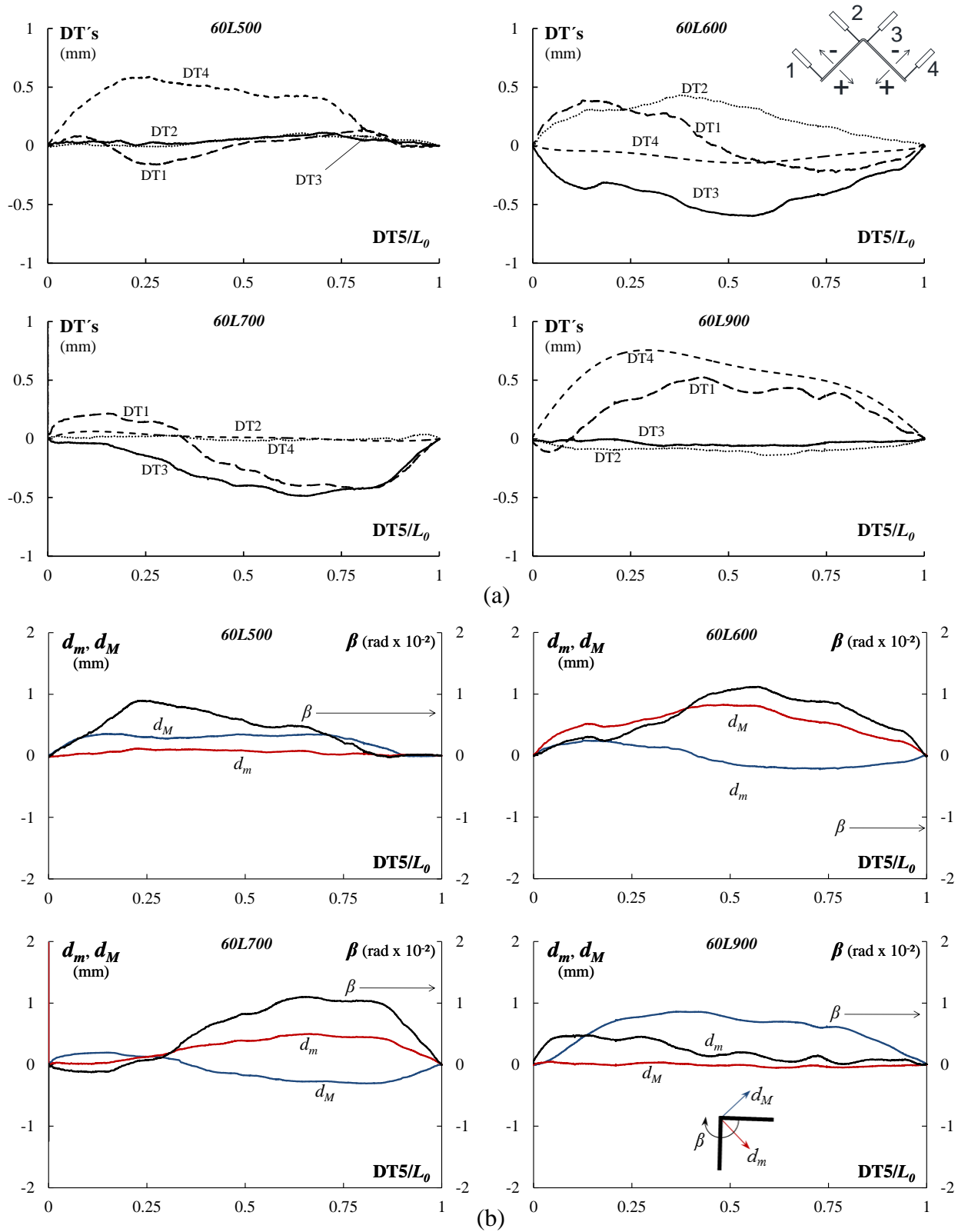


**Figure 11:** Initial displacement and rotation longitudinal profiles (horizontal coordinate normalized with respect to  $L_0$ ) concerning specimens 60L500-600-700-900: (a) DT1-4 readings and (b)  $\beta$ ,  $d_M$  and  $d_m$  values.

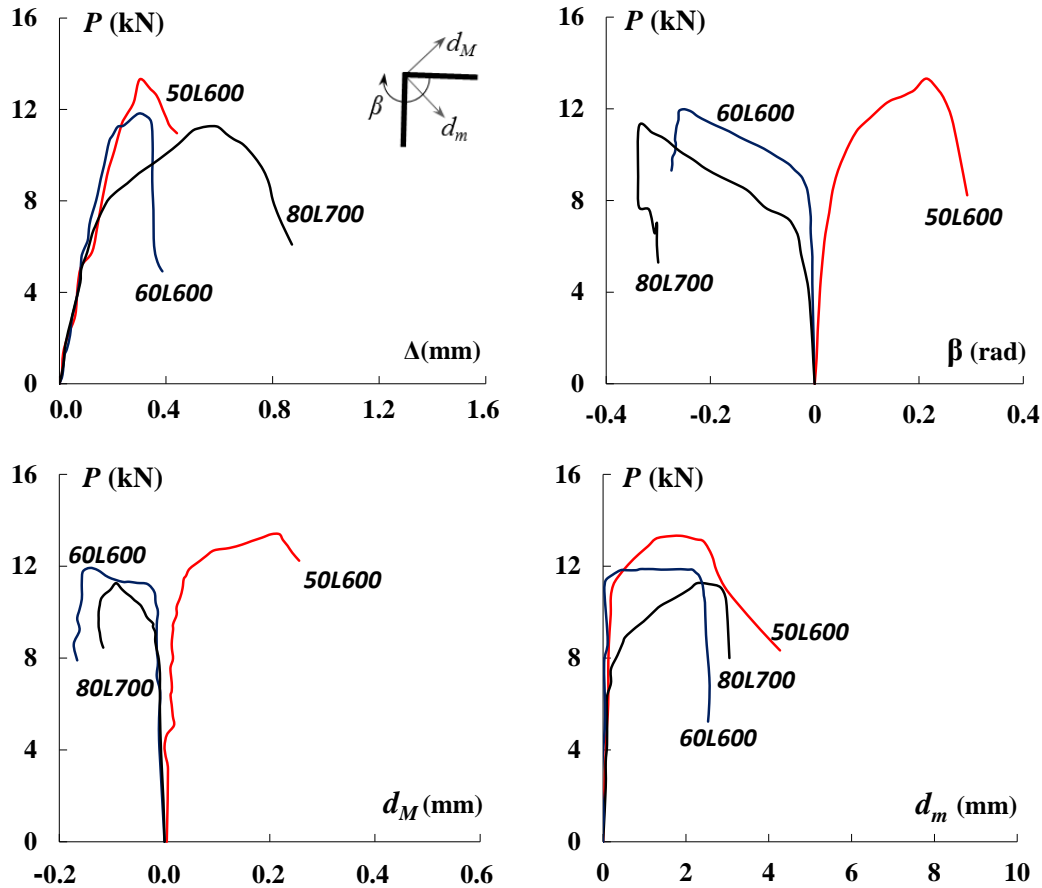


**Figure 12:** 50L600-60L600-80L700 column experimental equilibrium paths relating  $P$  to the axial shortening  $\Delta$  and the calculated mid-height torsional rotation  $\beta$  and displacements due to minor-axis ( $d_m$ ) and major-axis ( $d_M$ ) flexure.

#### 4.6.3 Failure Loads

Table 5 provides the column (i) experimental failure loads  $P_{u,Exp}$ , (ii) squash loads  $P_y$ , (iii) ratios  $P_{u,Exp}/P_y$  and (iv) failure mode natures. The values of  $P_y$  are based on (i) areas  $A$  obtained from the average values of the measured cross-section dimensions (disregarding the rounded corners) and (ii) the yield stress  $f_y=304.5\text{ MPa}$ , the average of the tensile coupon test results presented in Section 4.2. The specimens failed in either (i) a mode exhibiting highly predominant major-axis flexural-torsional deformations (termed “FT”) and (ii) a mode combining major-axis flexural-torsional deformations with visible minor-axis flexural ones (termed “FT+F”)<sup>12</sup>. The latter was found occur only for specimens 50L900, 50L1200 and 60L900, which are those combining the shortest leg widths with the longest lengths. This is just a logical consequence of the fact that the FT (critical) and F buckling loads are closer for such columns, thus leading to the occurrence of stronger interaction effects between the two buckling modes. Moreover, it should also be noticed that all specimens exhibit  $P_{u,Exp}/P_y$  ratios below 0.28, which is in accordance with their high slenderness values (plasticity plays a lesser role in the column failure). Finally, it is still worth noting that the failure loads corresponding to the repeated tested specimens (50L600 and 50L600-R) differ by about 2%, thus evidencing quite good test repeatability.

<sup>12</sup>The careful displacement measurements reveal that the specimens failing in FT modes also exhibit minor-axis flexure, which only appears very close to failure. Nevertheless, the  $d_m$  displacements are not visible by the naked eye, unlike those exhibited by the specimens failing in FT+F modes.

**Table 5:** Experimental results: column failure loads, squash loads and observed failure modes.

Column	$P_{u.Exp}$ (kN)	$P_y$ (kN)	$\frac{P_{u.Exp}}{P_y}$	Failure mode
50L600	13.32	46.87	0.28	FT
50L600-R	13.03	47.53	0.27	FT
50L900	11.43	47.13	0.24	FT+F
50L1200	12.27	47.98	0.26	FT+F
60L500	15.51	57.35	0.27	FT
60L600	11.82	57.82	0.20	FT
60L700	14.56	58.08	0.25	FT
60L900	10.31	57.41	0.18	FT+F
70L500	13.55	66.50	0.20	FT
70L600	12.90	68.38	0.19	FT
70L700	12.77	66.48	0.19	FT
70L900	12.82	67.26	0.19	FT
80L500	12.80	75.78	0.17	FT
80L600	12.65	76.34	0.17	FT
80L700	11.26	76.30	0.15	FT
80L900	9.04	76.19	0.12	FT
90L500	14.16	85.46	0.17	FT
90L600	11.61	86.81	0.13	FT
90L700	11.38	85.88	0.13	FT
90L900	10.07	85.69	0.12	FT

#### 4.6.4 Deformed configurations and failure modes

Figs. 13(a)-(b) concern specimen 80L500 and provide (i) its equilibrium path  $P$  vs.  $\Delta$  and (ii) the evolution of its deformed configuration during the test (*i.e.*, as the applied load increases) – the six deformed configuration shown in Fig. 13(b) correspond to the equilibrium states *I* to *VI* indicated by yellow circles on the equilibrium path depicted in Fig. 13(a). On the other hand, Figs. 14(a)-(c) and 15(a)-(b) show (i) the deformed configurations, at the onset of collapse ( $P \approx P_{u.Exp}$ ), of specimens 600L900, 700L900 and 700L600, (ii) a close view of the specimen 600L900 most deformed region just after collapse and (iii) a joint view of the deformed shapes of the four specimens with leg width  $b=90mm$  (90 series) after the load removal. The observation of these column deformed configurations makes it possible to conclude that:

- (i) The evolution of the specimen 80L500 deformed configuration, depicted in Fig. 13(b), nicely illustrates the emergence and development of predominantly torsional flexural-torsional deformations towards failure in a single half-wave FT mode, akin to the corresponding critical buckling mode<sup>13</sup>. The specimen remains almost undeformed until state *I* (about 20% of the failure load). However, beyond this stage flexural-torsional displacements become clearly visible and grow progressively until failure, which occurs at state *V*. After the peak load has been reached, the deformation becomes more pronounced, as illustrated by means of state *VI*.

<sup>13</sup>Of course, the designation “single half-wave” takes into account the two “quarter-waves” appearing near the specimen supports, which are fixed with respect to torsion and major-axis flexure. Moreover, there are also minute (not visible by the naked eye, but revealed by the displacement measurements) minor-axis flexural deformations due to the effective centroid shift effects (Dinis *et al.* 2012).

- (ii) The collapse mechanisms exhibited by all the specimens are triggered by the formation of “plastic hinges” at the one and three quarter-height cross-sections, as can be observed in Figs. 13(b-V) and 14(a)-(c) – numerical evidence of this feature was recently reported by Dinis *et al.* (2015).
- (iii) The specimens deformed configurations depicted in Fig. 15(b) make it possible to assess the amount of elastic deformation undergone by the compressed columns during the test, which is subsequently recovered after the load was removed – *e.g.*, it suffices to compare the deformed configurations displayed in Figs. 14(a)-(c) and 15(b).

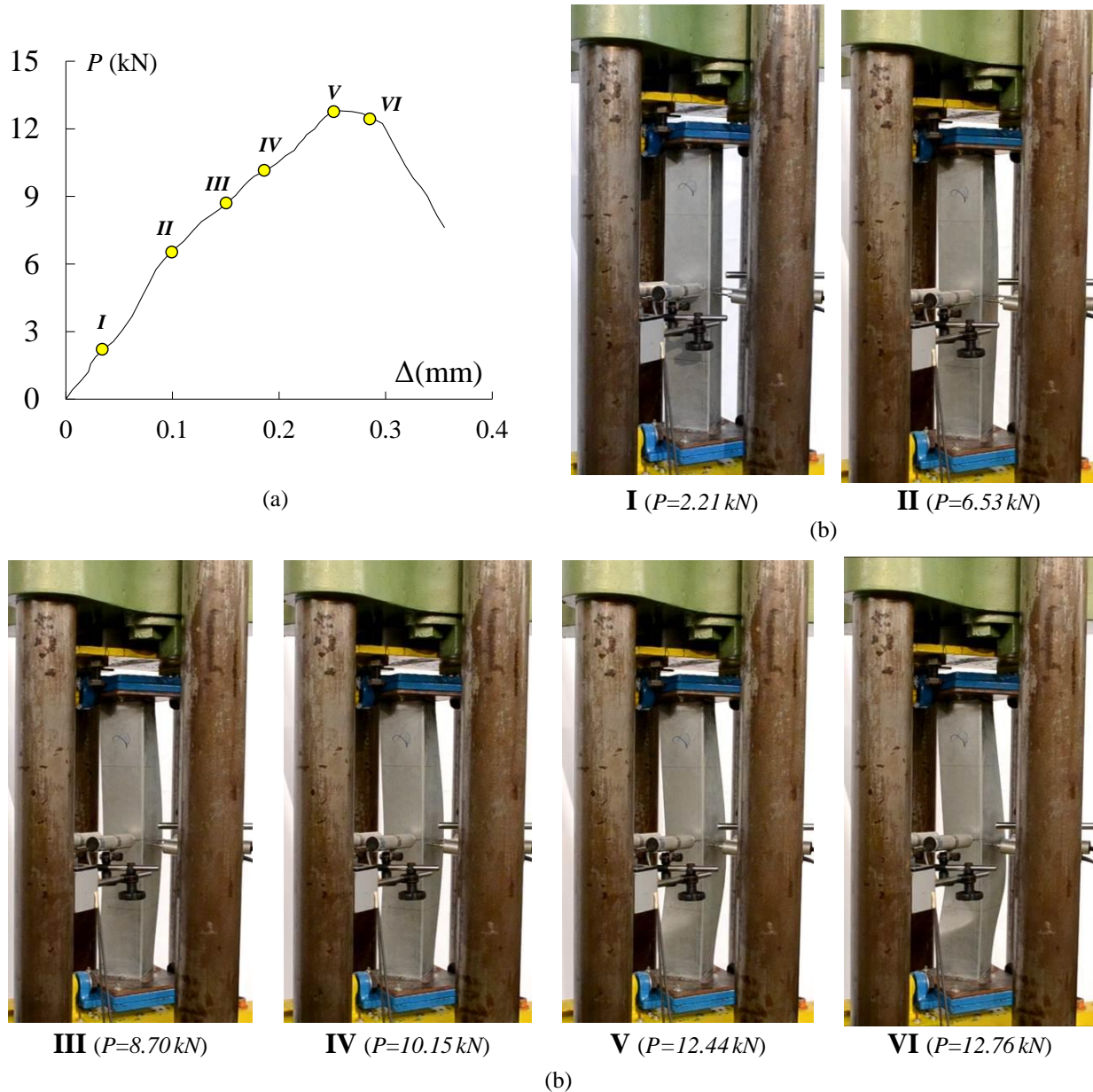


**Figure 13:** 80L500 specimen (a) equilibrium path  $P$  vs.  $\Delta$  and (b) deformed configuration evolution.



**Figure 14:** Deformed configurations at the onset of collapse of specimens (a) 600L900, (b) 700L900 and (c) 700L600.



**Figure 15:** (a) Close view of the most deformed region of specimen 600L900 just after collapse and (b) joint view of the specimens belonging to the 90 series after the load removal.

## 5. Numerical Simulations

After briefly addressing the main features of the ANSYS (SAS 2009) shell finite element (SFE) model adopted to perform the numerical simulation of the column tests, its validation is presented by comparing experimental results reported in Section 4.6 with the corresponding values provided by the column geometrically and materially non-linear analyses. Then, the (validated) SFE model is employed to analyze the columns identified in Table 2, in order to gather additional failure load data concerning slender pin-ended equal-leg angle columns.

### 5.1 ANSYS Shell Finite Element Model

The columns were discretized into SHELL181 elements (ANSYS nomenclature – 4-node shear deformable thin-shell elements with six degrees of freedom per node and full integration) – convergence studies showed that  $5\text{ mm} \times 5\text{ mm}$  meshes provide accurate results, while involving a reasonable computational effort. The analyses were performed by means of an incremental-iterative technique combining Newton-Raphson’s method with an arc-length control strategy.

All columns exhibited (i) an elastic-perfectly plastic material behavior (Prandtl-Reuss’s model: von Mises yield criterion and associated flow rule), characterized by  $E=205\text{ GPa}$ ,  $\nu=0.3$  and four yield stresses ( $f_y=304.5$  and  $f_y=250; 450; 600\text{ MPa}$ , respectively for the validation and parametric studies), (ii) pinned end supports materialized by attaching the member end sections to rigid end plates (thus ensuring full secondary warping and local displacement/rotation restraint) with prevented flexural displacements, major-axis flexural rotations and torsional rotations (pinned supports with cylindrical hinge, see Section 4.3), and (iii) initial imperfections either taken from the initial imperfection measurements (validation study) or combining a critical flexural-torsional component, with amplitude equal to  $10\%$  of the wall thickness  $t$ , and a non-critical minor-axis flexural component, with amplitude equal to  $L/1000$  (parametric study)<sup>14</sup> – value in line with the measurements reported for the specimens tested by Popovic *et al.* (1999) and made in the specimens tested in this work. Each buckling mode shape was determined by means of a preliminary ANSYS SFE buckling analysis, performed with exactly the same mesh employed to carry out the subsequent non-linear analysis – this procedure makes it very easy to “transform” the buckling analysis output into a non-linear analysis input. However, in the validation study, the initial geometrical imperfections considered were obtained through a procedure based on the Fourier series approximation of the measured (i) cross-section torsional rotation ( $\beta$ ), (ii) “horizontal” displacement ( $d_H$ ) and (iii) “vertical” displacement ( $d_V$ ) longitudinal profiles (see Fig. 11). In order to illustrate the quality of the output of this procedure, Figs. 16(a)-(b) compare the measured 50L600 column  $d_H$  and  $d_V$  longitudinal profiles with their approximations obtained by means of linear combination of trigonometric functions – it is clear that there is an excellent correlation. The three initial approximation longitudinal functions are then used to obtain the column “initially imperfect configuration” and incorporate it in the shell finite element mesh – when necessary, a linear displacement variation along the cross-section wall mid-line is assumed between the equally spaced leg nodes. Since the tensile coupon tests showed that the steel material behavior is clearly elastic-perfectly plastic (see Fig. 4), no strain-hardening was considered. Moreover, no residual stresses and/or corner effects were included in the analyses. The axial compression is applied through concentrated forces applied on the rigid end plate points corresponding to the end section centroids (the

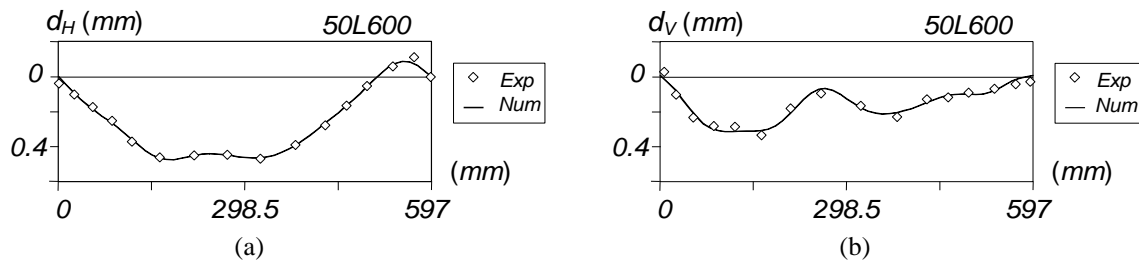


**Figure 16:** Comparison between the measured and approximated 50L600 column (a)  $d_H$  and (b)  $d_V$  displacement profiles.

<sup>14</sup>Although it was found that the shorter columns virtually insensitive to the minor-axis flexural imperfections (only the flexural-torsional imperfections are relevant), it was decided, for the sake of completion, that all the columns analyzed contained both flexural-torsional and minor-axis flexural initial imperfections. Moreover, note that the initial  $d_m$  values always “point” towards the cross-section corner, thus reinforcing the effective centroid shift effects (this is the most detrimental situation).

longitudinal displacement of one mid-height cross-section point is prevented). The above axial forces are always increased in small increments, by means of the ANSYS automatic load stepping procedure.

### 5.2 Validation Study

A fraction of the experimental results reported in Section 4.6 is now used to show the adequacy of the adopted ANSYS SFE model. Table 6 provides the data concerning the columns considered (specimens 50L600, 60L600 and 80L700), namely their (i) measured geometries and maximum initial displacement and rotation amplitudes, and (ii) experimental failure loads. Moreover, this table also includes the (i) column numerical failure loads and (ii) the percentage differences with respect to the experimental ones. On the other hand, Figs. 17(a)-19(b) show comparisons between the three specimen numerical and experimental (i) equilibrium paths ( $P$  vs.  $\Delta$ ,  $\beta$ ,  $d_m$ ,  $d_M$ ) (ii) failure modes (deformed shapes at the onset of collapse). The observation of these comparisons leads to the following comments:

- (i) The numerical post-buckling equilibrium paths are always reasonably close to the experimental ones and replicate very well their peak loads – the percentage differences never exceed 5%. Moreover, they provide confirmation of the occurrence of interaction between major-axis flexural-torsional and minor-axis flexural buckling – the column collapse modes combine significant mid-span rigid-body rotations ( $\beta > 0.2 \text{ rad}$ ) and displacements due to minor-axis bending ( $d_m$  – much larger than the  $d_M$ ).
- (ii) Although there is very good qualitative agreement between the numerical and experimental equilibrium paths, there are visible quantitative differences, namely those concerning the ductility prior to failure, which is considerably higher in the numerical results.
- (iii) There is a quite satisfactory match between the ANSYS failure modes and the observed collapse mechanisms: both are fairly symmetric and provide clear evidence of flexural-torsional deformations.
- (iv) The three specimen failure loads are safely and fairly accurately estimated by incorporating into the analyses initial geometrical imperfections combining a critical flexural-torsional component, with amplitude  $0.1t$ , and a non-critical minor-axis flexural component, with amplitude  $L/1000$ . Indeed, the failure loads obtained read  $P_{u,Num} = 12.28, 11.66, 11.21 \text{ kN}$ , for the 50L600, 60L600 and 80L700 columns, respectively – 8.9%, 1.3% and 0.4% below the corresponding experimental values.
- (v) On the basis of the above comparisons, it seems fair to conclude that the SFE model employed is able to capture adequately the geometrically and materially non-linear (post-buckling) behavior and strength of the short-to-intermediate pin-ended equal-leg angle columns under consideration. Therefore, this model will be used to perform the parametric study presented in the next section, aimed at gathering additional column failure loads, covering a wider slenderness range.

**Table 6:** Specimens considered in the validation study: (i) measured geometries and maximum initial displacement and rotation amplitudes, (ii) experimental and numerical failure loads, and (iii) percentage difference between them.

Column	$b$ (mm)	$t$ (mm)	$\theta_b$ (deg)	$L_0$ (mm)	$d_{m0}$ (mm)	$d_{M0}$ (mm)	$\beta_0$ (rad x $10^{-2}$ )	$P_{u,Exp}$ (kN)	$P_{u,Num}$ (kN)	$\frac{P_{u,Exp} - P_{u,Num}}{P_{u,Exp}}$
50L600	50.93	1.55	90	597	1.86	1.08E-03	3.1945	13.32	12.71	4.6%
60L600	61.5	1.58	90	596	0.673	5.97E-04	0.5359	11.82	11.68	1.2%
80L700	81.59	1.56	90	703	1.4145	2.75E-04	-1.3446	11.26	11.78	-4.9%

### 5.3 Parametric Study – Numerical Failure Loads

The aim of this section is to present the numerical failure load data gathered from the parametric study carried out, involving a total of 57 columns that correspond to all combinations of the 19 geometries and 3 yield stresses given in Table 2. Table 7 provides the column (i) numerical failure loads  $P_{u,Num}$ , (ii)

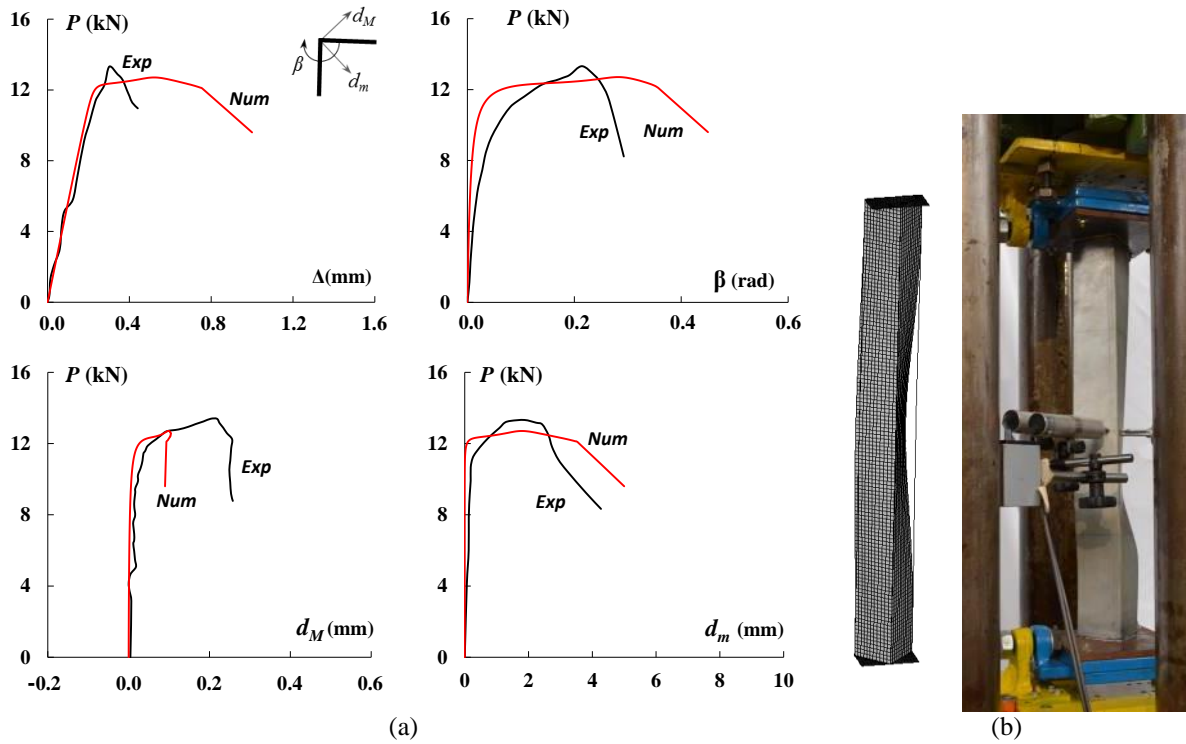


**Figure 17:** 50L600 column experimental and numerical (a) equilibrium paths relating  $P$  to the axial shortening  $\Delta$  and the mid-height torsional rotation  $\beta$  and displacements  $d_m$  and  $d_M$  flexure, and (b) collapse mechanisms.

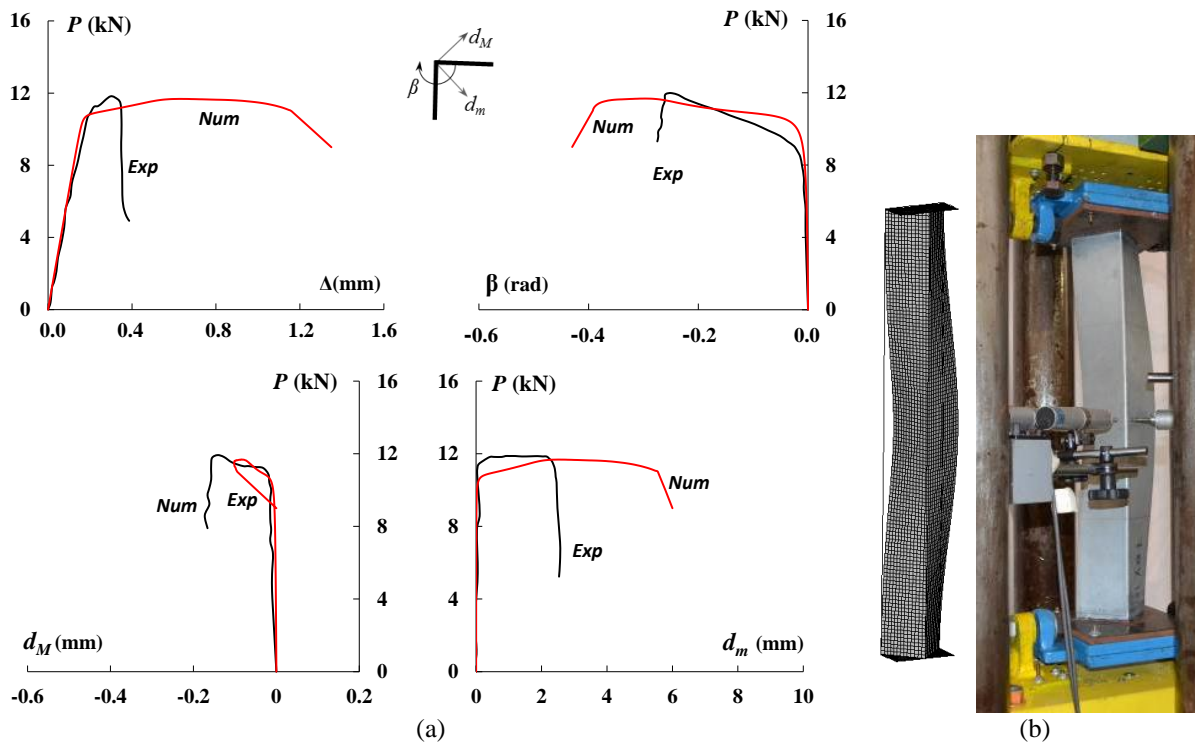


**Figure 18:** 60L600 column experimental and numerical (a) equilibrium paths relating  $P$  to the axial shortening  $\Delta$  and the mid-height torsional rotation  $\beta$  and displacements  $d_m$  and  $d_M$  flexure, and (b) collapse mechanisms.

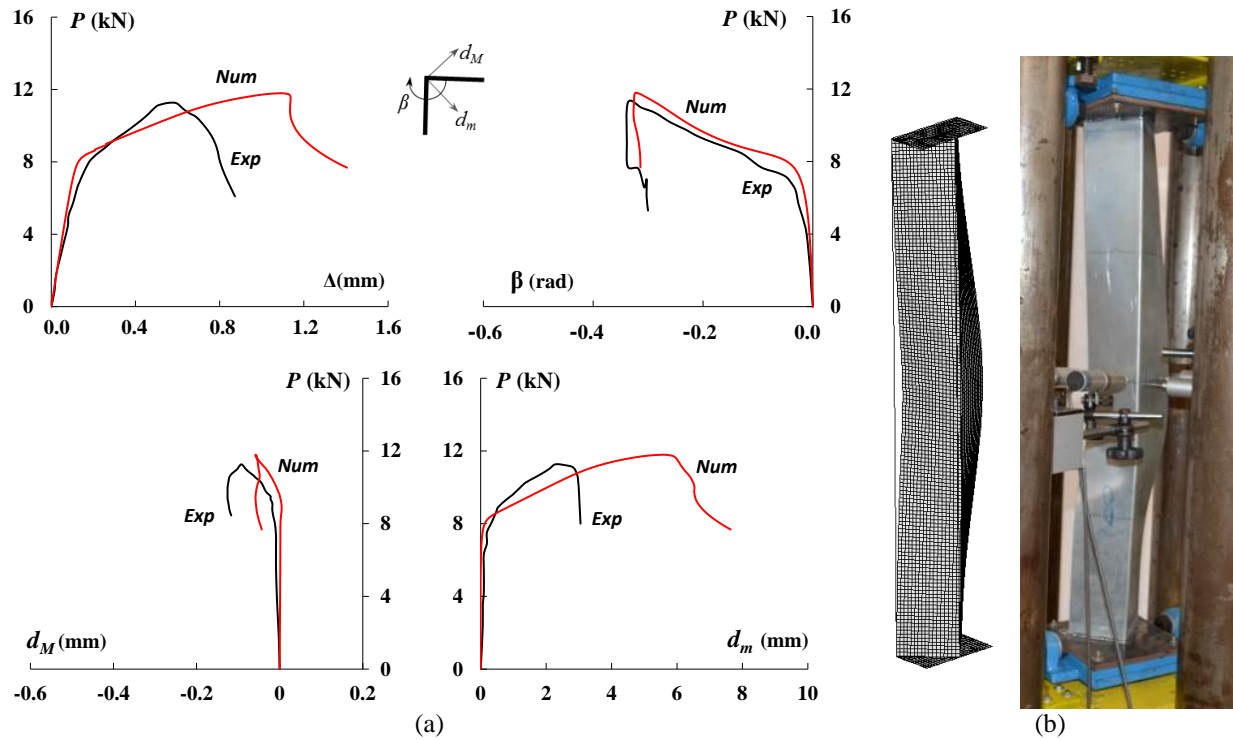


**Figure 19:** 80L700 column experimental and numerical (a) equilibrium paths relating  $P$  to the axial shortening  $\Delta$  and the mid-height torsional rotation  $\beta$  and displacements  $d_m$  and  $d_M$  flexure, and (b) collapse mechanisms.

**Table 7:** Parametric study: column (i) numerical failure loads, (ii) squash loads, (iii) ratios  $P_{u,Num}/P_y$  and (iv) slenderness values  $\lambda_{fie}$ .

Column designation	$P_y$ (kN)	$P_{u,Num}$ (kN)	$\frac{P_{u,Num}}{P_y}$	$\lambda_{fie}$	$P_y$ (kN)	$P_{u,Num}$ (kN)	$\frac{P_{u,Num}}{P_y}$	$\lambda_{fie}$	$P_y$ (kN)	$P_{u,Num}$ (kN)	$\frac{P_{u,Num}}{P_y}$	$\lambda_{fie}$
50L600	38.75	11.10	0.287	1.62	69.75	10.89	0.156	2.02	93.00	12.02	0.129	2.21
50L900		10.06	0.260	1.47		9.21	0.132	1.68		10.08	0.108	1.72
50L1200		8.98	0.232	1.27		7.90	0.113	1.30		8.98	0.097	1.30
60L500	46.50	11.10	0.239	1.97	83.70	11.29	0.135	2.56	111.60	13.32	0.119	2.88
60L600		10.70	0.230	1.97		11.11	0.133	2.51		12.22	0.109	2.80
60L700		10.33	0.222	1.95		9.87	0.118	2.44		11.15	0.100	2.68
60L900		9.61	0.207	1.86		9.04	0.108	2.24		9.67	0.087	2.38
70L500	54.25	11.18	0.206	2.28	97.65	10.64	0.109	2.98	130.20	13.77	0.106	3.38
70L600		10.75	0.198	2.30		9.89	0.101	2.98		13.51	0.104	3.34
70L700		10.34	0.191	2.30		9.76	0.100	2.93		11.75	0.090	3.26
70L900		9.43	0.174	2.24		9.20	0.094	2.77		9.65	0.074	3.01
80L500	62.00	11.33	0.183	2.57	111.60	11.20	0.100	3.38	148.80	13.84	0.093	3.85
80L600		10.98	0.177	2.62		9.89	0.089	3.41		13.30	0.089	3.86
80L700		10.63	0.171	2.63		9.08	0.081	3.40		12.46	0.084	3.81
80L900		9.67	0.156	2.60		8.66	0.078	3.28		10.15	0.068	3.61
90L500	69.75	11.35	0.163	2.84	125.55	12.07	0.096	3.75	167.40	13.56	0.081	4.28
90L600		11.12	0.159	2.91		10.59	0.084	3.82		13.14	0.078	4.34
90L700		10.88	0.156	2.95		9.47	0.075	3.84		12.69	0.076	4.33
90L900		10.14	0.145	2.95		8.13	0.065	3.77		10.82	0.065	4.19

squash loads  $P_y$ , (iii) ratios  $P_{u,Num}/P_y$  and (iv) slenderness values  $\lambda_{fte}$  – note that the column yield stresses  $f_y$  and DSM global strengths  $f_{ne}$  have already been given in Table 2. It is observed the columns analyzed cover a quite wide slenderness range ( $1.27 \leq \lambda_{fte} \leq 4.34$ ) and that, within each column series, the ratio  $P_{u,Num}/P_y$  decreases with the length, thus reflecting the growing relevance of instability effects.

## 6. Assessment of the Proposed DSM Design Approach

Attention is now turned to assessing the performance of the DSM-based design approach proposed by Dinis & Camotim (2015), already presented in Section 2. The ultimate strength predictions ( $f_{nfte}$ ) provided by this approach for the columns experimentally tested and numerically analyzed in this work are given in the tables included in Annex A, as well as the corresponding failure-to-predicted ultimate strength ratios  $f_u/f_{nfte}$  – while Table A.1 concerns the experimentally tested columns, Tables A.2 to A.4 deal with the numerically analyzed ones. Figs. 20(a)-(b) plot against  $\lambda_{fte}$ , the experimental and numerical  $f_u/f_{nfte}$  values (i) obtained in this work (grey circles) and (ii) previously available, as reported by Dinis & Camotim (2015) (white circles). Moreover, the indicators (averages, standard deviations and maximum/minimum values) concerning the failure loads (i) obtained in this work, (ii) reported by Dinis & Camotim (2015) and (iii) available (the whole set) are provided in Table 8 – in each case, separate indicators are given for the experimental, numerical and combined failure loads. The observation of the results presented in these figures and table prompts the following remarks:

- (i) The columns tested in the experimental campaign reported in this work exhibit high slenderness ( $\lambda_{fte}$ ) values, thus providing the intended complement to the previously available test results. As for the numerical results obtained in this work, they “mingle” quite well with the existing ones.
- (ii) The failure loads obtained in this work are very well predicted by the proposed DSM-based design approach. Indeed, the  $f_u/f_{nfte}$  averages and standard deviations are (ii<sub>1</sub>) 1.12/0.21 (experimental), (ii<sub>2</sub>) 1.09/0.09 (numerical) and (ii<sub>3</sub>) 1.10/0.12 (experimental + numerical). Moreover, the maximum and minimum  $f_u/f_{nfte}$  values read (ii<sub>1</sub>) 1.50/1.01 (experimental), (ii<sub>2</sub>) 1.27/0.94 (numerical) and (ii<sub>3</sub>) 1.50/0.94 (experimental + numerical).
- (iii) The above performance indicators are quite similar to those obtained for the failure loads reported by Dinis & Camotim (2015) – indeed, those dealing with the numerical  $f_u/f_{nfte}$  ratios are virtually identical. Concerning the experimental failure loads, those obtained in this work are all safely and

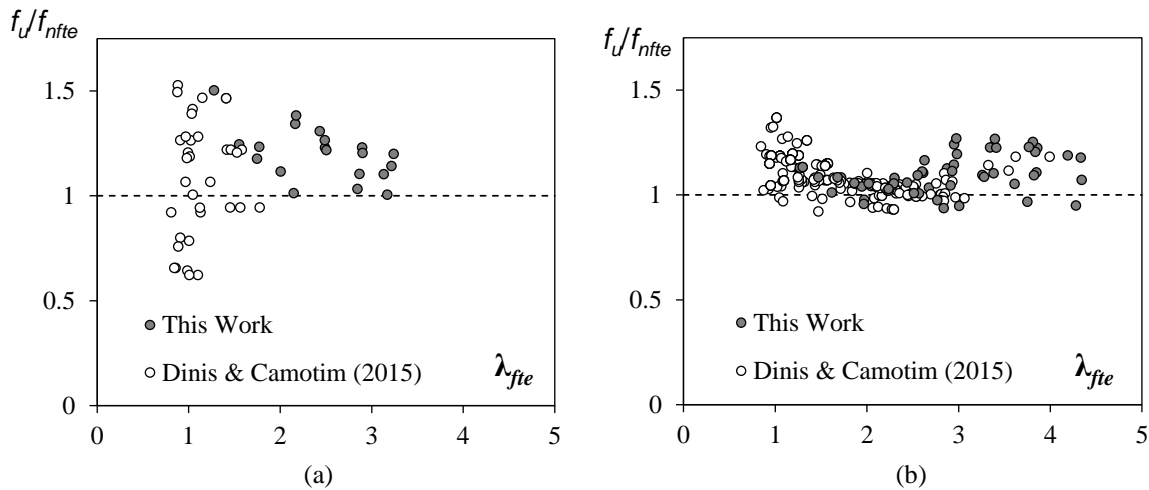


**Figure 20:** (a) Experimental and (b) numerical  $f_u/f_{nfte}$  vs.  $\lambda_{fte}$  plots concerning the values (i) obtained in this work and (ii) reported by Dinis & Camotim (2015).

**Table 8:** Averages, standard deviations and maximum/minimum values of  $f_u/f_{nfe}$  concerning the experimental, numerical and combined failure loads obtained in this work, reported by Dinis & Camotim (2015) and both (whole set).

$\frac{f_u}{f_{nfe}}$	This Work			Dinis & Camotim (2015)			Whole Set		
	Exp.	Num.	Exp + Num	Exp.	Num.	Exp + Num	Exp	Num.	Exp + Num
Mean	1.20	1.09	1.12	1.13	1.10	1.10	1.16	1.10	1.11
Sd. Dev.	0.13	0.09	0.11	0.25	0.09	0.13	0.22	0.09	0.12
Max	1.50	1.27	1.50	1.78	1.37	1.78	1.78	1.37	1.78
Min	1.01	0.94	0.94	0.81	0.92	0.81	0.81	0.92	0.81

reasonably accurately predicted (as attested by the  $1.20 f_u/f_{nfe}$  average), while large fractions of the values reported by other researchers are overestimated (severely in a few cases) or excessively underestimated –  $1.13 f_u/f_{nfe}$  average is a consequence of the high scatter ( $0.25$  standard deviation).

- (iv) In view of what was mentioned in the previous item, it is not surprising that the inclusion of the experimental and numerical failure loads obtained in this work causes only marginal changes in the  $f_u/f_{nfe}$  indicators determined by Dinis & Camotim (2015). Indeed, the maximum and minimum values remain the same and the average and standard deviation changes are minute: (iv<sub>1</sub>)  $+0.03/-0.03$  (experimental), (iv<sub>2</sub>)  $0.0/0.0$  (numerical) and (iv<sub>3</sub>)  $+0.01/-0.01$  (experimental + numerical). This implies that the failure loads obtained in this work are perfectly in line with their predecessors.

### 6.1 Load and Resistance Factor Design (LRFD)

This section addresses the evaluation of the LRFD (Load and Resistance Factor Design) resistance factor  $\phi$  associated with the proposed DSM-based design approach. According to the North American cold-formed steel specification (AISI 2012),  $\phi$  is calculated by the formula given in section F.1.1 of chapter F,

$$\phi = C_\phi (M_m F_m P_m) e^{-\beta_0 \sqrt{V_M^2 + V_F^2 + C_P V_P^2 + V_Q^2}} \quad \text{with} \quad C_P = \left(1 + \frac{1}{n}\right) \frac{m}{m-2}, \quad (20)$$

where (i)  $C_\phi$  is a calibration coefficient ( $C_\phi=1.52$  for LRFD), (ii)  $M_m=1.10$  and  $F_m=1.00$  are the mean values of the material and fabrication factor, respectively, (iii)  $\beta_0$  is the target reliability index ( $\beta_0=2.5$  for structural members in LRFD), (iv)  $V_M=0.10$ ,  $V_F=0.05$  and  $V_Q=0.21$  are the coefficients of variation of the material factor, fabrication factor and load effect, respectively, and (v)  $C_P$  is a correction factor that depends on the numbers of tests ( $n$ ) and degrees of freedom ( $m=n-1$ ). In order to evaluate  $\phi$  for the proposed DSM procedure, it is necessary to calculate  $P_m$  and  $V_P$ , the average and standard deviation of the  $f_u/f_{nfe}$  ratios – the  $f_u$  values are either experimental, numerical or experimental and numerical.

Table 9 shows the  $n$ ,  $C_P$ ,  $P_m$ ,  $V_P$  and  $\phi$  values obtained for the column failure load predictions provided by the DSM design approach for the experimental, numerical and whole failure data (i) obtained in this work and (ii) reported by Dinis and Camotim (2015). It is observed that:

- (i) The inclusion of the experimental and numerical failure load obtained in this work leads to  $\phi$  values that, with respect to those determined by Dinis & Camotim (2015), are either (i<sub>1</sub>) visibly higher (experimental –  $0.78$  to  $0.86$ ), (i<sub>2</sub>) identical (numerical –  $0.97$ ) or (i<sub>3</sub>) marginally higher (experimental and numerical –  $0.93$  to  $0.94$ ).
- (ii) The results obtained in this work reinforce the conclusion drawn by Dinis & Camotim (2015): there is solid evidence that  $\phi=0.85$  can be recommended for cold-formed steel angle columns designed with the proposed DSM-based approach (currently not the case – Ganesan & Moen 2012).

**Table 9:** LRFD  $\phi$  values according to AISI (2012) concerning the prediction of the experimental, numerical and combined failure loads obtained in this work, reported by Dinis & Camotim (2015) and both (whole set) by the proposed DSM design approach.

	This Work			Dinis & Camotim (2015)			Whole Set		
	Exp.	Num.	Exp + Num	Exp.	Num.	Exp + Num	Exp	Num.	Exp + Num
n	20	57	77	35	197	232	55	254	309
$C_p$	1.17	1.06	1.04	1.093	1.015	1.013	1.06	1.01	1.01
$P_m$	1.20	1.09	1.12	1.129	1.096	1.101	1.16	1.10	1.11
$V_p$	0.13	0.09	0.11	0.235	0.091	0.129	0.22	0.09	0.12
$\phi$	1.01	0.97	0.97	0.78	0.97	0.93	0.86	0.97	0.94

### 6.2 Modification of the Proposed DSM Design Approach

This section assesses the consequences of a slight modification in the proposed DSM design approach, which consists of altering the definition of the  $\Delta_f$  appearing in Eq. (1) to

$$\Delta_f = \frac{f_{bt} - f_{crft}}{f_{bt}} \times 100 \quad . \quad (21)$$

The alteration consists of changing the denominator from  $f_{crft}$  to  $f_{bt}$ , which corresponds to having  $\Delta_f$  defined as “the relative drop of the critical flexural-torsional buckling stress with respect to the purely torsional bifurcation stress”. Note that the new  $\Delta_f$  values fall a little below the old ones – obviously, the difference increases with the column length, *i.e.*, with the value of  $(f_{bt} - f_{crft})$ .

Tables 10 and 11 present the (i) indicators of the  $f_u/f_{nftc}$  ratios and (ii) LRFD  $\phi$  values obtained with the  $\Delta_f$  definition given in Eq. (21). The comparison between the results presented in Tables 8-9 and 10-11 make it possible to conclude that the above modification leads to:

- (i) Practically identical  $f_u/f_{nftc}$  averages and standard deviations values – the corresponding changes are, for the whole set of results, (i<sub>1</sub>)  $-0.01/0.0$  (experimental), (i<sub>2</sub>)  $-0.01/0.0$  (numerical) and (i<sub>3</sub>)  $-0.01/0.0$  (experimental + numerical). Moreover, the maximum and minimum values change by (i<sub>1</sub>)  $-0.02/0.0$  (experimental), (i<sub>2</sub>)  $-0.01/0.0$  (numerical) and (i<sub>3</sub>)  $-0.02/0.0$  (experimental + numerical).
- (ii) Absolutely identical  $\phi$  values for all the sets of results considered.

Therefore, the incorporation of the new (more clear) definition of  $\Delta_f$  in the proposed DSM design approach has virtually no impact on the its merits, as attested by the fact that the  $f_u/f_{nftc}$  indicators either remain identical or exhibit almost imperceptible changes.

**Table 10:** Averages, standard deviations and maximum/minimum values of  $f_u/f_{nftc}$  obtained with  $\Delta_f$  given by Eq. (21).

$\frac{f_u}{f_{nftc}}$	This Work			Dinis & Camotim (2015)			Whole Set		
	Exp.	Num.	Exp + Num	Exp.	Num.	Exp + Num	Exp	Num.	Exp + Num
Mean	1.20	1.09	1.12	1.12	1.09	1.10	1.15	1.09	1.10
Sd. Dev.	0.12	0.09	0.11	0.25	0.09	0.13	0.22	0.09	0.12
Max	1.50	1.27	1.50	1.76	1.36	1.76	1.76	1.36	1.76
Min	1.00	0.94	0.94	0.80	0.92	0.80	0.81	0.92	0.81

**Table 11:** LRFD  $\phi$  values according to AISI (2012) obtained with  $\Delta_f$  given by Eq. (21).

	This Work			Dinis & Camotim (2015)			Whole Set		
	Exp.	Num.	Exp + Num	Exp.	Num.	Exp + Num	Exp	Num.	Exp + Num
n	20	57	77	35	197	232	55	254	309
$C_p$	1.17	1.06	1.04	1.093	1.015	1.013	1.06	1.01	1.01
$P_m$	1.20	1.09	1.12	1.122	1.092	1.096	1.15	1.09	1.10
$V_p$	0.12	0.09	0.11	0.250	0.088	0.126	0.22	0.09	0.12
$\phi$	1.01	0.97	0.97	0.78	0.97	0.93	0.86	0.97	0.94

## 7. Concluding Remarks

This work mainly reported the results of an experimental investigation on the behavior and collapse of cold-formed steel short-to-intermediate pin-ended equal-leg angle columns with high slenderness values, which was carried out to fill a gap detected by Dinis & Camotim (2015), in the context of the development and performance assessment of a DSM-based design procedure for such members. After briefly reviewing this DSM procedure, the paper addressed the selection of the geometries of (i) the column specimens to be fabricated and tested at COPPE (Federal University of Rio de Janeiro) and also (ii) additional columns to be analyzed numerically by means of ANSYS SFE simulations. Then, detailed descriptions of the experimental, displacement measurements (prior to and during the test) and test procedure were provided, followed by the presentation and discussion of the results obtained, including the (i) initial geometrical imperfection measurements, (ii) equilibrium paths relating the applied load to column displacements, (iii) deformed configurations (including the collapse modes) and (iv) failure loads.

Next, a representative sample of those experimental results was used to validate a previously developed SFE model, which was subsequently employed to obtain additional numerical failure load data concerning the pin-ended angle columns under scrutiny. Then, it was shown that the experimental and numerical failure loads obtained in this work could be efficiently (safely and reasonably accurately) predicted by the DSM design approach proposed by Dinis & Camotim (2015), thus providing further evidence of its merits. Finally, the whole column failure load data available (comprising the values determined in this work and those taken from Dinis & Camotim 2015), totaling 55 (20+35) experimental and 254 (57+197) numerical values, were used to assess the performance of the proposed DSM design approach. It was found that indicators of the failure-to-predicted ultimate strength ratio ( $f_u/f_{nfe}$ ) are very close (slightly better) to those reported by Dinis & Camotim (2015), thus ensuring the same quality and reliability levels. In particular, it was confirmed (even reinforced) that the LRFD resistance factor  $\phi=0.85$ , currently prescribed by AISI (2012) for the design of compression members, can also be safely adopted for the failure load prediction of pin-ended angle by the proposed DSM design approach (angle columns are current explicitly excluded from the application of this resistance factor).

Finally, it was show that a slight modification incorporated in the DSM design procedure, related to the definition of the parameter  $\Delta_f$ , has no impact on the its merits, since the quality and reliability of the failure load predictions remain practically unchanged.

## Acknowledgments

The authors gratefully acknowledge the financial support of CNPq (Brazilian National Council of Technological and Scientific Development), through the research project “Numerical and Experimental

Analyses of Cold-Formed Steel Structural Members” (MEC/MCTI/CAPES/CNPq/FAPs No. 61/2011), submitted and approved in the context of the Program “Science without Borders”.

## References

- ABNT (Brazilian Association of Technical Standards) (2012). *Steel-Coated Coils and Plates with Zinc or Zinc-Iron Alloy by Hot-Dip Continuous Process Immersion – Part 1: Requirements*, ABNT NBR 7008-1, Rio de Janeiro. (Portuguese).
- ABNT (Brazilian Association of Technical Standards) (2015). *Metallic Materials – Tensile Testing – Part 1: Method of Test at Room Temperature*, ABNT NBR ISO 6892-1, Rio de Janeiro. (Portuguese).
- AISI (American Iron and Steel Institute) (2012). *North American Specification (NAS) for the Design of Cold-Formed Steel Structural Members*, AISI-S100-12, Washington DC.
- ASTM (American Society for Testing and Materials) (2011). *Standard Specification for Steel Sheet, Zinc-Coated (Galvanized) or Zinc-Iron Alloy-Coated (Galvannealed) by the Hot-Dip Process*, ASTM. A653, West Conshohocken.
- ASTM (American Society for Testing and Materials) (2015). *Test Methods for Tension Testing of Metallic Materials*, ASTM. E8/E8M-15a, West Conshohocken.
- Bebiano R, Silvestre N, Camotim D (2008). “GBTUL – a code for the buckling analysis of cold-formed steel members”, *Proceedings of 19<sup>th</sup> International Specialty Conference on Recent Research and Developments in Cold-Formed Steel Design and Construction* (St. Louis, 14-15/10), R. LaBoube, W.-W. Yu (eds.), 61-79.
- Chodraui GMB, Shifferaw Y, Malite M, Schafer BW (2006). “Cold-formed steel angles under axial compression”, *Proceedings of 18<sup>th</sup> International Specialty Conference on Cold-Formed Steel Structures* (Orlando, 26-27/10), R. LaBoube, W.W. Yu (eds.), 285-300.
- Cruz R (2015). *Experimental Analysis and Design of Slender Pin-Ended Cold-Formed Steel Equal-Leg Angle Columns*, M.A.Sc. Thesis in Structural Engineering, COPPE, Federal University of Rio de Janeiro, 2015. (Portuguese)
- Dinis PB, Camotim D (2015). “A novel DSM-based approach for the rational design of fixed-ended and pin-ended short-to-intermediate thin-walled angle columns”, *Thin-Walled Structures*, **87**(February), 158-182.
- Dinis PB, Camotim D, Silvestre N (2010). “On the local and global buckling behaviour of angle, T-section and cruciform thin-walled columns and beams”, *Thin-Walled Structures*, **48**(10-11), 786-797.
- Dinis PB, Camotim D, Silvestre N (2012). “On the mechanics of angle column instability”, *Thin-Walled Structures*, **52**(March), 80-89.
- Ellobody E, Young B (2005). “Behavior of cold-formed steel plain angle columns”, *Journal of Structural Engineering* (ASCE), **131**(3), 469-478.
- Ganesan K, Moen CD (2012). “LRFD resistance factor for cold-formed steel compression members”, *Journal of Constructional Steel Research*, **72**(May), 261-266.
- Kitipornchai S, Chan SL (1987). “Nonlinear finite-element analysis of angle and tee beam-columns”, *Journal of Structural Engineering* (ASCE), **113**(4), 721-739.
- Kitipornchai S, Albermani FGA, Chan SL (1990). “Elastoplastic finite-element models for angle steel frames”, *Journal of Structural Engineering* (ASCE), **116**(10), 2567-2581.
- Maia WF, Neto JM, Malite M (2008). “Stability of cold-formed steel simple and lipped angles under compression”, *Proceedings of 19<sup>th</sup> International Specialty Conference on Cold-Formed Steel Structures* (St. Louis, 26-27/10), R. LaBoube, W.W. Yu (eds.), 111-125.
- Mesacasa Jr. EC (2012). *Structural Behavior and Design of Cold-Formed Steel Angle Columns*, M.A.Sc. Thesis in Structural Engineering, School of Engineering at São Carlos, University of S. Paulo, Brazil. (Portuguese)
- Mesacasa Jr. E, Dinis PB, Camotim D, Malite M (2012). “Flexural buckling of simply supported columns with ‘rigid end links’ – the key to interpret pin-ended angle column test results?”, *USB Key Drive Proceedings of Structural Stability Research Council Annual Stability Conference* (Grapevine – 17-21/4), paper 4.
- Mesacasa Jr. E, Dinis PB, Camotim D, Malite M (2014). “Mode-interaction in thin-walled equal-leg angle columns”, *Thin-Walled Structures*, **81**(August), 138-149.
- Popovic D, Hancock GJ, Rasmussen KJR (1999). “Axial compression tests of cold-formed angles”, *Journal of Structural Engineering* (ASCE), **125**(5), 515-523.
- Rasmussen KJR (2005). “Design of angle columns with locally unstable legs”, *Journal of Structural Engineering* (ASCE), **131**(10), 1553-1560.

- Rasmussen KJR (2006). "Design of slender angle section beam-columns by the direct strength method", *Journal of Structural Engineering* (ASCE), **132**(2), 204-211.
- Swanson Analysis Systems Inc. (SAS) (2009). *Ansys Reference Manual* (vrs. 12).
- Shifferaw Y, Schafer BW (2011). "Behavior and design of cold-formed steel lipped and plain angles", *USB Proceedings of SSRC Annual Stability Conference* (Pittsburgh, 10-14/5).
- Young B (2004). "Tests and design of fixed-ended cold-formed steel plain angle columns", *Journal of Structural Engineering* (ASCE), **130**(12), 1931-1940.

ANNEX A: PIN-ENDED COLUMN EXPERIMENTAL AND NUMERICAL FAILURE LOAD DATA

**Table A.1:** Pin-ended column critical stresses, experimental ultimate strengths and their DSM estimates ( $f_y=304.4\text{ MPa}$ )

Column	L	$f_{bf}$	$f_{cft}$	$f_{cre}$	$\Delta_f$	a	b	c	d	$\beta$	$f_{nfte}$	$f_u$	$f_{nfte}$	$\lambda_{fte}$	$\frac{f_u}{f_{nfte}}$
50L600	597	9816.6	77.3	565.3	0.30	0.47	0.15	0.42	0.74	0.54	70.12	86.49	70.12	1.77	1.23
50L600-R	607	9521.9	79.0	548.0	0.31	0.48	0.15	0.42	0.74	0.55	71.00	83.53	71.00	1.75	1.18
50L900	903	4299.2	75.3	247.1	0.67	0.55	0.16	0.35	0.77	0.59	59.21	73.74	59.21	1.55	1.25
50L1200	1204	2441.1	75.3	140.3	1.19	0.65	0.17	0.24	0.81	0.66	51.67	77.66	51.67	1.28	1.50
60L500	508	19621.4	58.1	1144.7	0.11	0.43	0.15	0.52	0.73	0.47	61.45	82.50	61.45	2.16	1.34
60L600	596	14362.2	56.7	836.1	0.15	0.44	0.15	0.54	0.66	0.50	61.44	62.21	61.44	2.15	1.01
60L700	700	10722.0	52.5	626.5	0.18	0.45	0.15	0.50	0.68	0.48	55.11	76.23	55.11	2.18	1.38
60L900	905	6224.9	53.3	362.3	0.32	0.48	0.15	0.42	0.74	0.48	48.91	54.55	48.91	2.01	1.12
70L500	505	26542.2	45.2	1562.5	0.06	0.42	0.15	0.55	0.75	0.41	50.56	62.16	50.56	2.49	1.23
70L600	602	19182.1	43.3	1131.5	0.08	0.42	0.15	0.52	0.76	0.40	47.08	57.33	47.08	2.51	1.22
70L700	694	14046.1	42.2	826.9	0.11	0.43	0.15	0.53	0.73	0.42	46.32	58.58	46.32	2.49	1.26
70L900	899	8541.6	40.0	503.8	0.18	0.44	0.15	0.52	0.66	0.44	44.33	58.01	44.33	2.43	1.31
80L500	502	35596.1	34.9	2112.4	0.04	0.41	0.15	0.66	0.64	0.41	46.57	51.41	46.57	2.87	1.10
80L600	603	24724.9	33.3	1466.8	0.05	0.41	0.15	0.60	0.71	0.38	40.96	50.40	40.96	2.90	1.23
80L700	703	18168.8	32.1	1078.0	0.07	0.42	0.15	0.55	0.75	0.36	37.26	44.86	37.26	2.90	1.20
80L900	908	10861.6	30.9	644.3	0.11	0.43	0.15	0.52	0.74	0.36	35.03	36.16	35.03	2.85	1.03
90L500	500	44905.3	29.6	2678.1	0.02	0.41	0.15	0.75	0.55	0.42	45.70	50.39	45.70	3.13	1.10
90L600	595	31821.9	28.3	1899.7	0.03	0.41	0.15	0.68	0.62	0.39	40.53	40.74	40.53	3.17	1.01
90L700	706	22459.0	26.7	1339.2	0.04	0.41	0.15	0.62	0.68	0.35	35.35	40.35	35.35	3.22	1.14
90L900	897	14062.9	24.9	837.8	0.07	0.42	0.15	0.55	0.75	0.32	29.85	35.84	29.85	3.24	1.20

Note 1: dimensions in mm, stresses in MPa

Note 2: the above  $\Delta_f$  values and DSM estimates are based on the average measured cross-section dimensions (see Table 3)

**Table A.2:** Pin-ended column critical stresses, numerical ultimate strengths and their DSM estimates ( $f_y=250\text{ MPa}$ )

Column	L	$f_{bf}$	$f_{cft}$	$f_{cre}$	$\Delta_f$	a	b	c	d	$\beta$	$f_{nfte}$	$f_u$	$f_{nfte}$	$\lambda_{fte}$	$\frac{f_u}{f_{nfte}}$
50L600	600	9367.0	80.0	586.1	0.32	0.48	0.15	0.42	0.74	0.59	70.79	71.63	70.79	1.62	1.01
50L900	900	4163.1	77.2	260.5	0.71	0.56	0.16	0.34	0.77	0.62	59.91	64.93	59.91	1.47	1.08
50L1200	1200	2341.7	75.9	146.5	1.26	0.67	0.17	0.23	0.82	0.66	51.34	57.97	51.34	1.27	1.13
60L500	500	19423.4	59.0	1214.8	0.11	0.43	0.15	0.53	0.73	0.52	61.12	59.67	61.12	1.97	0.98
60L600	600	13488.5	57.0	843.6	0.16	0.44	0.15	0.54	0.65	0.54	60.12	57.53	60.12	1.97	0.96
60L700	700	9909.9	55.8	619.8	0.21	0.45	0.15	0.44	0.73	0.50	53.41	55.52	53.41	1.95	1.04
60L900	900	5994.9	54.4	374.9	0.34	0.48	0.15	0.41	0.74	0.52	48.90	51.65	48.90	1.86	1.06
70L500	500	26437.4	45.1	1653.2	0.06	0.42	0.15	0.55	0.75	0.45	49.29	51.52	49.29	2.28	1.05
70L600	600	18359.3	43.1	1148.1	0.09	0.42	0.15	0.52	0.76	0.44	45.81	49.54	45.81	2.30	1.08
70L700	700	13488.5	41.9	843.5	0.12	0.43	0.15	0.53	0.72	0.45	45.21	47.66	45.21	2.30	1.05
70L900	900	8159.7	40.6	510.3	0.19	0.45	0.15	0.49	0.68	0.46	42.62	43.45	42.62	2.24	1.02
80L500	500	34530.5	36.1	2159.1	0.04	0.41	0.15	0.65	0.65	0.44	45.39	45.70	45.39	2.57	1.01
80L600	600	23979.5	34.1	1499.3	0.05	0.41	0.15	0.58	0.72	0.41	40.07	44.29	40.07	2.62	1.11
80L700	700	17617.6	32.9	1101.6	0.07	0.42	0.15	0.54	0.76	0.39	36.78	42.87	36.78	2.63	1.17
80L900	900	10657.5	31.6	666.4	0.11	0.43	0.15	0.52	0.73	0.40	35.07	38.99	35.07	2.60	1.11
90L500	500	43702.6	29.9	2732.3	0.03	0.41	0.15	0.74	0.55	0.45	43.47	40.70	43.47	2.84	0.94
90L600	600	30349.0	27.9	1897.4	0.03	0.41	0.15	0.68	0.62	0.41	38.11	39.85	38.11	2.91	1.05
90L700	700	22297.2	26.7	1394.0	0.04	0.41	0.15	0.62	0.68	0.38	34.09	38.99	34.09	2.95	1.14
90L900	900	13488.5	25.4	843.3	0.07	0.42	0.15	0.54	0.76	0.35	29.28	36.33	29.28	2.95	1.24

Note: dimensions in mm, stresses in MPa

**Table A.3:** Pin-ended column critical stresses, numerical ultimate strengths and their DSM estimates ( $f_y=450\text{ MPa}$ )

<i>Column</i>	<i>L</i>	$f_{bf}$	$f_{cft}$	$f_{cre}$	$\Delta_f$	<i>a</i>	<i>b</i>	<i>c</i>	<i>d</i>	$\beta$	$f_{nfte}$	$f_u$	$f_{nfte}$	$\lambda_{fte}$	$\frac{f_u}{f_{nfte}}$
50L600	600	9367.0	80.0	586.1	0.32	0.48	0.15	0.42	0.74	0.48	73.57	77.57	73.57	2.02	1.05
50L900	900	4163.1	77.2	260.5	0.71	0.56	0.16	0.34	0.77	0.54	59.99	65.03	59.99	1.68	1.08
50L1200	1200	2341.7	75.9	146.5	1.26	0.67	0.17	0.23	0.82	0.64	51.17	57.97	51.17	1.30	1.13
60L500	500	19423.4	59.0	1214.8	0.11	0.43	0.15	0.53	0.73	0.41	65.46	71.61	65.46	2.56	1.09
60L600	600	13488.5	57.0	843.6	0.16	0.44	0.15	0.54	0.65	0.44	65.13	65.68	65.13	2.51	1.01
60L700	700	9909.9	55.8	619.8	0.21	0.45	0.15	0.44	0.73	0.41	56.58	59.93	56.58	2.44	1.06
60L900	900	5994.9	54.4	374.9	0.34	0.48	0.15	0.41	0.74	0.43	50.58	52.01	50.58	2.24	1.03
70L500	500	26437.4	45.1	1653.2	0.06	0.42	0.15	0.55	0.75	0.35	53.10	63.44	53.10	2.98	1.19
70L600	600	18359.3	43.1	1148.1	0.09	0.42	0.15	0.52	0.76	0.34	49.04	62.24	49.04	2.98	1.27
70L700	700	13488.5	41.9	843.5	0.12	0.43	0.15	0.53	0.72	0.36	48.63	54.15	48.63	2.93	1.11
70L900	900	8159.7	40.6	510.3	0.19	0.45	0.15	0.49	0.68	0.39	45.63	44.45	45.63	2.77	0.97
80L500	500	34530.5	36.1	2159.1	0.04	0.41	0.15	0.65	0.65	0.35	50.59	55.82	50.59	3.38	1.10
80L600	600	23979.5	34.1	1499.3	0.05	0.41	0.15	0.58	0.72	0.32	43.75	53.62	43.75	3.41	1.23
80L700	700	17617.6	32.9	1101.6	0.07	0.42	0.15	0.54	0.76	0.31	39.65	50.24	39.65	3.40	1.27
80L900	900	10657.5	31.6	666.4	0.11	0.43	0.15	0.52	0.73	0.32	37.66	40.93	37.66	3.28	1.09
90L500	500	43702.6	29.9	2732.3	0.03	0.41	0.15	0.74	0.55	0.37	50.23	48.61	50.23	3.75	0.97
90L600	600	30349.0	27.9	1897.4	0.03	0.41	0.15	0.68	0.62	0.33	43.06	47.10	43.06	3.82	1.09
90L700	700	22297.2	26.7	1394.0	0.04	0.41	0.15	0.62	0.68	0.31	37.74	45.48	37.74	3.84	1.21
90L900	900	13488.5	25.4	843.3	0.07	0.42	0.15	0.54	0.76	0.28	31.57	38.77	31.57	3.77	1.23

Note: dimensions in *mm*, stresses in *MPa***Table A.4:** Pin-ended column critical stresses, numerical ultimate strengths and their DSM estimates ( $f_y=600\text{ MPa}$ )

<i>Column</i>	<i>L</i>	$f_{bf}$	$f_{cft}$	$f_{cre}$	$\Delta_f$	<i>a</i>	<i>b</i>	<i>c</i>	<i>d</i>	$\beta$	$f_{nfte}$	$f_u$	$f_{nfte}$	$\lambda_{fte}$	$\frac{f_u}{f_{nfte}}$
50L600	600	9367.0	80.0	586.1	0.32	0.48	0.15	0.42	0.74	0.44	74.91	78.06	74.91	2.21	1.04
50L900	900	4163.1	77.2	260.5	0.71	0.56	0.16	0.34	0.77	0.53	60.02	65.03	60.02	1.72	1.08
50L1200	1200	2341.7	75.9	146.5	1.26	0.67	0.17	0.23	0.82	0.64	51.17	57.97	51.17	1.30	1.13
60L500	500	19423.4	59.0	1214.8	0.11	0.43	0.15	0.53	0.73	0.37	67.84	76.39	67.84	2.88	1.13
60L600	600	13488.5	57.0	843.6	0.16	0.44	0.15	0.54	0.65	0.40	67.68	67.65	67.68	2.80	1.00
60L700	700	9909.9	55.8	619.8	0.21	0.45	0.15	0.44	0.73	0.38	58.06	60.06	58.06	2.68	1.03
60L900	900	5994.9	54.4	374.9	0.34	0.48	0.15	0.41	0.74	0.41	51.20	52.01	51.20	2.38	1.02
70L500	500	26437.4	45.1	1653.2	0.06	0.42	0.15	0.55	0.75	0.31	55.21	68.00	55.21	3.38	1.23
70L600	600	18359.3	43.1	1148.1	0.09	0.42	0.15	0.52	0.76	0.31	50.76	62.24	50.76	3.34	1.23
70L700	700	13488.5	41.9	843.5	0.12	0.43	0.15	0.53	0.72	0.33	50.35	55.11	50.35	3.26	1.09
70L900	900	8159.7	40.6	510.3	0.19	0.45	0.15	0.49	0.68	0.36	46.93	44.45	46.93	3.01	0.95
80L500	500	34530.5	36.1	2159.1	0.04	0.41	0.15	0.65	0.65	0.32	53.48	59.22	53.48	3.85	1.11
80L600	600	23979.5	34.1	1499.3	0.05	0.41	0.15	0.58	0.72	0.29	45.73	55.97	45.73	3.86	1.22
80L700	700	17617.6	32.9	1101.6	0.07	0.42	0.15	0.54	0.76	0.28	41.13	51.51	41.13	3.81	1.25
80L900	900	10657.5	31.6	666.4	0.11	0.43	0.15	0.52	0.73	0.30	38.88	40.93	38.88	3.61	1.05
90L500	500	43702.6	29.9	2732.3	0.03	0.41	0.15	0.74	0.55	0.34	54.02	51.26	54.02	4.28	0.95
90L600	600	30349.0	27.9	1897.4	0.03	0.41	0.15	0.68	0.62	0.30	45.75	49.02	45.75	4.34	1.07
90L700	700	22297.2	26.7	1394.0	0.04	0.41	0.15	0.62	0.68	0.28	39.67	46.71	39.67	4.33	1.18
90L900	900	13488.5	25.4	843.3	0.07	0.42	0.15	0.54	0.76	0.25	32.69	38.85	32.69	4.19	1.19

Note: dimensions in *mm*, stresses in *MPa*